Characterization of Nanofilter Arrays for Small Molecule Separation

by

Hansen Chang Bow

B.S. Electrical Engineering and Computer Sciences, 2004
University of California, Berkeley

Submitted to the Department of Electrical Engineering and Computer Science in partial fulfillment of the requirements for the degree of

Masters of Science in Electrical Engineering and Computer Science
at the
MASSACHUSETTS INSTITUTE OF TECHNOLOGY

June 2006

Signature of Author: _____
Department of Electrical Engineering and Computer Science
May 25, 2006

Certified by: _____
Jongyoon Han
Assistant Professor of Electrical Engineering and Computer Science
rvisor

Accepted by: _____
Smith
Professor of Electrical Engineering and Computer Science
Chairman, Committee for Graduate Students

Characterization of Nanofilter Arrays for Small Molecule Separation

by

Hansen Chang Bow

Submitted to the Department of Electrical Engineering and Computer Science on May 25, 2006, in partial fulfillment of the requirements for the degree of Masters of Science in Electrical Engineering and Computer Science

Abstract

Experimental studies were performed to evaluate methods of improving separation resolution and speed in microfabricated nanofilter arrays. Experiment parameters investigated include electric field strength, nanofilter geometry, and buffer concentration. DNA polymers of size 25-1000 base pairs were the subject of our study.

We concluded that increasing electric field strength resulted in inferior separation for larger DNA polymers (400-1000 bp). Additionally, we quantified the improvement in resolution of smaller nanofilter pores and lower buffer concentration. A theoretical model based on Macrotransport Theory was developed to estimate average species velocity and peak dispersion.

Thesis Supervisor: Jongyoon Han
Title: Assistant Professor of Electrical Engineering and Computer Science

Acknowledgments

I would like to thank Professor Han for being my research mentor and teacher. His passion, resourcefulness, and patience have always been qualities I try to emulate. I am especially grateful for his encouragement when experiments are successful and his suggestions and willingness to help when experiments do not work out as we had hoped.

I would also like to thank Jianping Fu for guiding me through the fabrication process and discussing various aspects of biomolecule separation. Current and past lab members have also helped me immensely with my research and become good friends. They include Pan Mao, Arnaud LeCoguic, Noel Reyes González, Ying-Chih Wang, and Yong-Ak Song. The staff at MTL's ICL were enjoyable to work with and extremely supportive.

I will be forever grateful to the teachers who have provided me the foundation to what I do today and who have broadened and challenged my thinking. I am also indebted to my parents and my family for encouraging me to do what interested me and brought me happiness.

Finally, this research is made possible with the support of funding sources NIH (GM68762, EB005743), SMA-II FRP-1, and DuPont-MIT Alliance Graduate Fellowship.

Contents

Chapter 1

Introduction

In parallel with the development of microelectronics and integrated circuits, the field of Microelecromechanical Systems (MEMS) has expanded from focusing mainly on pressure sensors and automobile accelerometers to presently the large areas encompassing relevant devices in medicine, optics, imaging, and positioning[1]. One of the applications of this technology is in the area of biology, termed BioMEMS: microfabrication has enabled the creation of devices on the length scale of cells (μm) and large biomolecules (10 nm), such as DNA[2]. Advantages of BioMEMS compared to traditional bio-analysis methods include faster preparation and analysis times, smaller sample requirements, integration of multiple steps on one device, and increased sensitivity.

Within BioMEMS, much research has been carried out during the past decade on separating biomolecules, such as carbohydrates, proteins, and DNA[3]. The characteristics that these separation methods rely on include size[4], charge[5], isoelectric point[6], binding affinity[7], and diffusivity[8]. The unique aspect of these separation methods is that they do not require the use of conventional sieving gels, such as polyacrylamide or agarose. These separations are accomplished in free solution, which facilitates sample recovery.

Separation of DNA has been extensively investigated in microfluidic devices. The separation of large DNA (> 10 kbp) in free solution has been accomplished with hydrodynamic chromatography[9], entropic traps[4], and pulsed-fields electrophoresis in the presence of posts[10]. Additionally, the separation of small (< 1 kbp) DNA in these devices has also been demonstrated without the use of gels. Using the same device geometry as Han et al. for separating large DNA[4], Fu et al. recently demonstrated separation of small DNA (< 1000 bp)[11] and proteins.

While separation of small biomolecules using microfabricated nanofilters has been demonstrated, further optimization is critically needed with respect to the following three objectives. First, these devices currently cannot separate natural proteins, carbohydrates, or hormones. The ability to separate these molecules on a microfabricated chip could lead to cheaper and more accurate screening and diagnostic medical devices. Second, to achieve better separation, we must understand and characterize the sieving process. The resolution achieved by a separation method depends on two factors: selectivity and dispersion. While selectivity in these devices has been addressed by Fu et al.[12], dispersion has not. Third, a theoretical model is necessary for understanding and predicting both selectivity and dispersion in different device geometries and experimental conditions.

In this thesis we characterize nanofilter molecular separation systems theoretically and experimentally with these three goals in mind. In Chapter 2, we first provide a concise description of the

concepts relevant to this work and briefly review relevant literature. In Chapter 3, we detail the specific materials and methods used in our experiments. In Chapter 4, we develop a basic model of ensemble velocity and dispersion based on Macrotransport Theory[13]. The following three chapters provide experimental results and discussions regarding the three aspects of nanofilter separation that we analyze: electric field strength, structural dimensions of the array, and buffer concentration. We conclude by summarizing our results and suggest future directions for research on nanofilter arrays.

Chapter 2

Background

When an electric potential is applied across a liquid containing charged particles, the particle movement that results is primarily a combination of electrophoresis and bulk electroosmosis. We briefly describe electrokinetic phenomena by providing a foundation with Debye length and then explaining electrophoresis and electroosmosis. More detailed reviews on electrokinetic phenomena[14,15] and DNA/electrophoresis[14] can be found elsewhere.

Electrokinetic Phenomena

Debye Length

When a charged surface is in contact with an electrolyte solution, counter-ions, ions oppositely charged with respect to the surface, will be attracted to it while co-ions will be repelled. The distance over which this effect occurs is called the electrical double layer, and the Debye length is a measure of its thickness:

$$\lambda_D \equiv \sqrt{\frac{\varepsilon RT}{F^2 \sum_{i=1}^{n} z_i^{\,2} c_{i\infty}}}$$

where ε is the permittivity of the liquid, R is the gas constant, T is the temperature, F is the Faraday constant, z_i is the charge of ion i, and $c_{i\infty}$ is the concentration of ion i far from the surface. The Debye length is proportional to the inverse of the square root of the ionic strength. Intuitively, greater concentration of ions results in greater shielding capacity, decreasing the Debye length. Outside the electrical double layer, the solution is electrically neutral.

Using the Debye-Hückel approximation, the electric potential in the solution is

$$\phi = \phi_w \exp(-\frac{x}{\lambda_D})$$

where x represents the distance from the charged surface and ϕ_w is the potential at the charged surface. From the Boltzmann distribution, the concentration of ion i in the solution is

$$c_i = c_{i\infty} \exp(\frac{-z_i F\phi}{RT})$$

where $c_{i\infty}$ is the concentration of ion i far from the surface. For a monovalent co-ion, the location x where ϕ equals 26 mV is the location where the concentration decays to 1/e of its value far from the surface, since RT/F = 26 mV at room temperature. In addition to the Debye length, this distance may be used to characterize the co-ion exclusion distance.

The potential at the wall may not be the most appropriate for analyzing experimental results, since there is usually a layer of ions permanently adsorbed to the wall. The distance over which the ions are fixed is called the Stern layer. The zeta potential, ζ, is the potential at the fluid slip plane just outside the Stern layer.

Electrophoresis

Electrophoresis occurs when an electric field causes a charged object to move with respect to a stationary liquid. A simple model for the particle velocity for relatively small Debye lengths compared to particle size is given by the Helmholtz-Smoluchowski equation.

$$U = \frac{\varepsilon\zeta E}{\mu}$$

where E is the transverse electric field and μ is the liquid viscosity. This model does not take into account the viscous drag created by the electroosmotic movement of the counterions, the increased conductivity immediately around the particle that reduces the effective electric field, or the dipole that is established from the non-spherical shape of the counter-ion cloud. From this equation, the electrophoretic velocity is independent of particle size for a given surface potential.

Electroosmosis

In contrast to electrophoresis, electroosmosis occurs when the liquid nearby a stationary charged object in solution moves in the presence of an electric field. This effect is caused by mobile ions in the electrical double layer migrating toward the oppositely charged electrode. The ion migration drags adjacent liquid by viscous forces, which results in overall liquid flow.

The electroosmotic flow profile between parallel charged plates is

$$u = -\frac{\varepsilon\zeta}{\mu}\left(1 - \exp(-|a-y|/\lambda_D)\right)E$$

where the plates are located at ±a. In the limit when the gap between the plates is large relative to the Debye length, i.e. for large a/λ_D, the electroosmotic flow velocity is effectively constant throughout the channel cross section. The value of this constant is again given by the Helmholtz-Smoluchowski equation

$$U = -\frac{\varepsilon \zeta E}{\mu}$$

Separation of DNA and Other Biomolecules

DNA electrophoresis

DNA is a polymer consisting of a sequence of base pair monomers. The double helix can be approximated as a cylinder with a 2.0 nm diameter and a rise/bp of 0.34 nm. When the contour length, the end to end length of a DNA molecule stretched linearly, is much greater than l_p = 50 nm ≈ 150 bp, the persistence length of DNA, its conformation is a random walk of step $l = 2l_p$ = 100 nm[14]. The approximate radius of this DNA molecule is given by the radius of gyration, R_g.

$$R_g^2 \equiv \frac{1}{N}\sum_{n=1}^{N}\left\langle (R_n - R_{cm})^2 \right\rangle$$
$$= \frac{1}{6} N l^2$$

where N = contour length / l, R_n is the location of segment n, and R_{cm} is the location of the chain's center of mass. When the contour length of DNA is shorter than l_p, DNA can be approximated as a rigid rod of length 0.34 × number of bp.

The negatively charged phosphate groups of DNA contribute 2 negative charges per bp to the overall charge of the molecule in neutral to alkaline pH. At the 8.3 pH used in our experiments, DNA is negatively charged. Therefore, in free solution under the influence of an electric field, they are dragged toward the anode.

Overview of Free-Solution DNA Separation in Microdevices

With the Human Genome Project (HGP) as stimulus, starting in the 1990s there has been an intense interest in developing microfluidic devices that can efficiently carry out Sanger sequencing of DNA. As was implied in the Electrophoresis section, the free solution mobility of long DNA polymers is independent of size. Although there have been efforts to attach molecular parachutes to the ends of these strands to create differences in mobility, this method has not generally been successful in separating DNA beyond 150 bp[15]. Traditional methods of separating DNA based on size evolved from 1950s methods of separating proteins and RNA. Agarose or acrylamide gels in containers with a length scale of 10 cm are typically used. These gels act as a sieve and smaller DNA fragments travel faster in the presence of an electric field. This method is still the most popular in typical biology laboratories today.

A major improvement to conventional gel electrophoresis, which was spurred by the human genome project, is capillary gel electrophoresis (CGE). During the 1990s, researchers experimented with ways of filling a microfluidic channel with a sieving gel[16]. This method provided improvements in the areas of sample amount, speed, ease of use, and integration of multiple preparation steps over traditional agarose or acrylamide separation techniques. The HGP, completed in 2003, primarily relied on this method.

Although capillary gel electrophoresis has been successful, filling a microfluidic channel with gel is not an easy process. Furthermore, this filling requirement makes integration with other processing steps on the same microfabricated device difficult. Because of these limitations, researchers have also

developed gel-free sieving structures in microfabricated devices[17]. Gel-free systems also enable sample collection. The separation mechanisms in gel-free microfluidic separation systems can be categorized into three broad categories: hydrodynamic chromatography, diffusivity, and sieving.

In hydrodynamic chromatography, each class of molecules samples different fluid streamlines with a unique probability distribution. For example, the center of a microfluidic channel travels faster than the edges due to viscous shear and no-slip at the walls. Large molecules will tend to sample the center flow stream more, since they are sterically hindered from sampling the edges. Thus large molecules travel faster. Blom et al. have used pressure to separate polystyrene beads[18]; Pennathur and Santiago used electric field to separate proteins based on charge repulsion from the wall[5]; and Iki et al. have used both electric field and pressure to separate DNA from 120 to 23130 bp[19]. Building on these one dimensional separation methods, two dimensional separation schemes were developed that could continuously separate and collect the separated particles. Huang et al. created a two-dimensional array of posts, which deflects particles laterally based on size[20]. Takagi et al. also created a device that sends particles to different channels by first pushing them against a wall and then having them follow their corresponding fluid streamline[21]. In all of these hydrodynamic chromatography separation methods, achieving high resolution is difficult. Fundamentally, in a parabolic flow profile, e.g. plane Poiseuille flow, the fastest particle can travel at a maximum of 1.5 times the speed of the slowest particle.

Another method of separating biomolecules in gel-free microfabricated devices exploits particles' diffusivity differences. The separation process is based on the concept of a ratchet: particles can only go forward, not back. Small particles travel faster because they diffuse forward faster than larger particles. To achieve the ratchet effect, Bader et al. created a periodic array of parallel alternating electrodes, with the distance between one electrode and its two neighbors being highly unequal[22]. The electric field would be switched on and off. Once a particle crosses the oppositely charged electrode when the electric field is off, it would be pushed forward to the next electrode when the field came back on. Similar in idea, van Oudenaarden and Boxer created a two dimensional array of diffusion barriers and used pressure-driven flow to separate non-polar phospholipids[23]. In both of these methods, high resolution is difficult to achieve, because diffusivity for a sphere depends only weakly on mass ($\sim M^{-1/3}$).

A third method of separating biomolecules in microfabricated devices is sieving. An array of small pores is created, and molecules are separated based on their ability to cross each pore. One of the pioneering studies of the class of devices was performed by Volkmuth and Austin. They created a two-dimensional array of pillars that was able to separate large DNA based on its ability to reptate through the array[24]. Huang et al. used asymmetric pulsed fields and a two-dimensional array of pillars to separate and collect DNA 61-209 kbp[25]. Han and Craighead created a channel with alternating depths that was also able to separate large (5 -160 kb) DNA[26]. Interestingly, in both this study and one-dimensional movement in the array of pillars larger DNA moved faster than smaller DNA. Using a similar device geometry as Han and Craighead, Fu et al. demonstrated separation of small DNA (100-1000 bp) and proteins[27]. Their method of separation involves smaller particles entering the shallow region more easily than larger particles, which results in greater velocity. They have also demonstrated two-dimensional separation and sample collection based on the same principles[28].

In this work, our eventual goal is to optimize Fu et al.'s nanofilter array[12] to separate even smaller particles, such as carbohydrates with sizes on the order of 10 bp of DNA. We determined that other methods of separation, such as hydrodynamic chromatography and diffusion, were not able to yield the resolution these carbohydrates required. As a precursor step, we used DNA as a model molecule to explore methods of increasing separation resolution. To achieve this goal, we experimented with electric field strength, device structure parameters, and buffer concentration.

Chapter 3

Materials and Methods

The materials and methods described in this chapter are used throughout this thesis. Only exceptions are mentioned in later chapters.

Reagents

TBE Buffer

Tris-Borate-EDTA (TBE) buffer was obtained from Sigma Aldrich. After dilution with the indicated amount of deionized water, which produced TBE 5×, the solution contained 0.445 M Tris-borate and 10 mM EDTA at pH 8.3. Different buffer concentrations were created by further diluting with deionized water.

YOYO-1 Labeled DNA

Fifty μl of the buffer planned for the experiment, 0.4 μl Invitrogen YOYO-1 dye, and 2.5 μg of either Invitrogen or New England Biolabs DNA were mixed together and left in the dark for 1 hour before use. This stoichiometry resulted in a 1:10 dye to DNA base-pair ratio.

Microfluidic Device

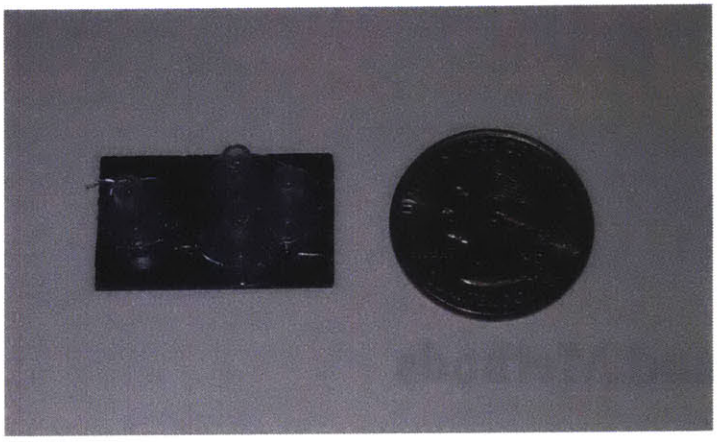

Figure 3.1: Photograph of device after attachment of reservoirs.

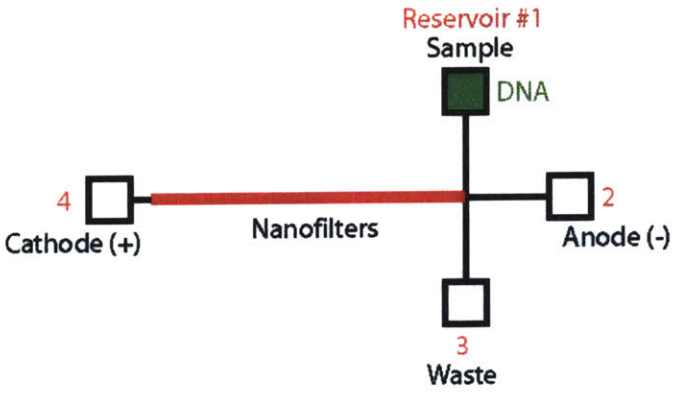

Figure 3.2: Schematic of reservoir numbering and purpose. Refer to Figure 3.1 for a photograph of the device.

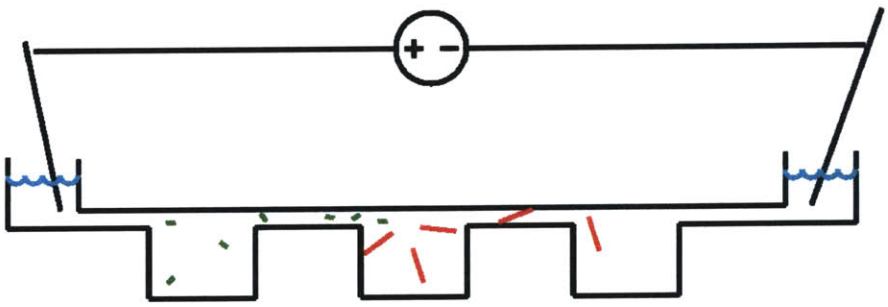

Figure 3.3: Schematic of nanofilter region connecting reservoirs 4 and 2. The green and red rods represent smaller and larger DNA respectively. The smaller DNA moves faster through the nanofilters.

The fabrication methods for the devices used in this thesis are detailed in Fu et al[11]. Specifics regarding the bonding of the pyrex cover to the etched silicon are detailed in Mao et al[29]. The periodicity of the shallow and deep regions for the devices used in this thesis is 1 μm. Immediately after device fabrication, a small amount of TBE 1× buffer was deposited in the access holes of the chip. Through capillary action, the buffer filled the device's channels within minutes. The devices were then stored in TBE 1× until needed.

To prepare a device for experiments, reservoirs were first attached to the access holes. The reservoirs consisted of a shortened TipOne 0.1-10 μl Natural Pipet Tips tip affixed with Amazing Goop Plumbing Contact Adhesive and Sealant. The reservoirs were then filled with TBE 1× and covered with Parafilm Laboratory Film to prevent evaporation until use.

The experiments in Chapter 7 regarding buffer concentration were done with devices fabricated by Jianping Fu, since they could withstand higher voltages without bubble formation as mentioned next.

Remark: Bubble formation

Air bubbles violently appeared in the microfluidic channels of the devices used in Chapters 3 and 4 when the voltage was increased beyond 30 v / cm. We speculate not enough insulating oxide covered the semi-conductive silicon substrate in certain locations, leading to electrical conductance through the channel. This defect may be produced by debris during the fabrication etch step creating silicon spikes. Subsequently, these spikes were not adequately converted into silicon dioxide during the oxidation step.

Hydrogen and oxygen gas are generated at the electrodes when a current flows through water. The conductive locations inside the channel effectively became electrodes, and hydrogen or oxygen was generated at those locations. These bubbles interrupted both the electric field and the path of the DNA in the separation region. At this point, the experiment was be aborted.

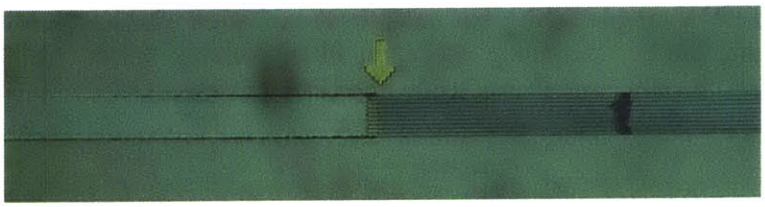

Figure 3.4: Photograph of bubbles toward the end of the separation region. The bubbles are 1/5 the figure width from the right. The device dimensions are 60/240 nm.

Remark: Filling

Devices with 40 nm shallow regions did not fill with TBE buffer. We speculate adverse surface conditions caused this problem. We attempted to use de-gassed buffer. We also tried biasing the silicon substrate. Neither of these efforts was successful.

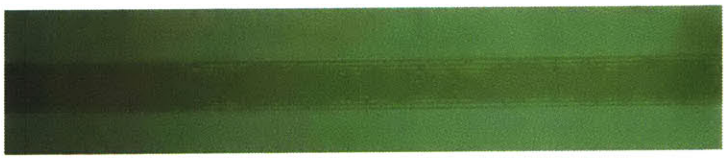

Figure 3.5: Photograph of unsuccessful device filling. The device dimensions are 40/160 nm.

Equipment

Voltage

Voltages were supplied by a Labsmith HVS448 3000D High Voltage Sequencer. The output voltages were connected to 100 kΩ resistors to prevent fluctuation at low voltages (< 50 V). The voltages supplied were observed to be accurate within 0.5 V of the desired value.

The nominal voltage used in each experiment was calculated based on the voltages applied at the four reservoirs, Figure 3.2. To calculate the voltage at the intersection, we ignored the voltage applied at reservoir 4, since the resistance from the intersection to reservoir 4 is much larger than that to reservoirs 1, 2, and 3. Reservoirs 1, 2, and 3 are about equidistant from the intersection, so the voltage at the intersection is 2/3 the value applied at reservoirs 1 and 3, which are always equal in the experiments. Thus the voltage across the separation region is the voltage at reservoir 4 subtract 2/3 the voltage at reservoir 3. For example, if the voltages at reservoirs 1, 2, 3, and 4 are 15, 0, 15, and 50 V, the voltage we indicate is 50 – 2/3 * 15 = 40 V/cm.

Illumination

An Olympus Optical Co. Model U-LH100HGAPO Mercury Lamp was used to provide large-scale illumination. For intensity measurements, a National Laser Company Argon Ion 488 nm laser provided more concentrated and less noisy illumination.

Microscope

An Olympus IX-71 inverted microscope was used to view the microfluidic channels. To quantify the YOYO-1 labeled DNA sample, which has an optimal excitation wavelength at 491 nm and emission wavelength at 509 nm, the corresponding excitation filter, dichroic mirror, and emission filters were chosen. For intensity vs. time measurements, a 40× objective lens was used.

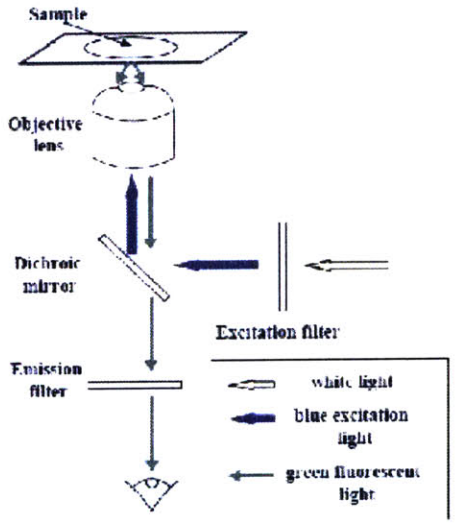

Figure 3.6: Illustration of sample fluorescence illumination. From LeCoguic et al.[30]

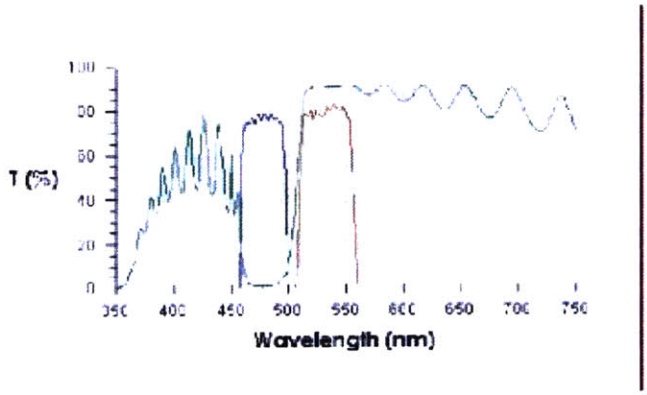

Figure 3.7: Filter transmittance vs. wavelength. Blue: excitation; red: emission; green: dichroic mirror. Adapted from LeCoguic et al.[30]

Data Acquisition and Processing

Images were captured on a PCO CCD Imaging SensiCam Camera and analyzed using Scanalytics' IPLab software. For all of the experiments, the image capture location was 0.5 cm from the start of the nanofilter region. Images were recorded every 0.5 s using 200 ms exposure. Curve-fitting was done using OriginLab Origin 7 software. From the curve-fitting, the mean velocity and standard deviation of the elution profiles were extracted.

To obtain the normalized mobility plots from the mobility data, all values were divided by the zero-size mobility. The zero-size mobility was extrapolated by linear least squares fitting of the first three data values. Typically these corresponded to 100, 200, and 300 bp or 50, 150, and 300 bp.

Experiment Procedure

Buffer Concentration Equilibration inside Channels

Before the actual experiments, the original buffer (TBE 1×) was removed from the reservoirs and the buffer planned for the experiments loaded. The device was then covered with Parafilm. Reservoir-specific platinum wires were rinsed with deionized water, ethanol, and deionized water again before insertion into the reservoirs through the Parafilm. Twenty Five volts were then applied across the nanofilter region for at least 12 hours. This voltage generates electroosmotic flow, which equilibrates the buffer concentration inside the channels.

Reservoir Preparation

Reservoirs are numbered, as shown in Figure 3.2. The buffer in reservoir 1 is replaced with the labeled DNA sample. The other reservoirs are replaced with buffer of the specified concentration. The reservoirs are re-covered with Parafilm. The reservoir-specific platinum wires, which prevent contamination, are inserted through the Parafilm.

Experiment Execution

To load the DNA, 20 volts were applied to reservoir 3 while the other reservoirs were grounded for at least 15 minutes. Once the intensity at the intersection was determined to be high enough (typically the maximum intensity was greater than 1000 units when illuminated by the mercury lamp through a 40 × objective using an amplification value of 3 and 4 × 4 binning in IPLab) the experiment was started.

Typically, an experiment consisted of 5 minutes of loading, 5 or 10 seconds of injection, and 2 hours of running. The timer is started at the same time as injection. After ensuring that the DNA has entered the separation region and is migrating through the nanofilters, the microscope stage is positioned at the intensity measurement location (typically next to marked location at center of the channel, 0.5 cm from the injection location). The light source is then changed from the mercury lamp to the argon-ion laser, and recording commences.

After an experiment, the nanofilter region is checked to ensure that it is free of DNA. If the channel is clear, the next experiment can proceed.

Chapter 4

Characterization of Velocity and Dispersion in Nanofilter Arrays Based on Macrotransport Theory

The separation resolution of a particular device and set of running conditions is critically determined by the average velocity and dispersion of the groups of molecules we attempt to separate. As a guide to more effective separations, we develop a theoretical model that attempts to predict the velocity and dispersion of groups of molecules.

One method of modeling the periodic nanofilter array is based on Macrotransport Theory. An excellent reference is Brenner and Edwards' *Macrotransport Processes*[13]. In Macrotransport Theory, which is effectively a generalization of Taylor-Aris dispersion, the micro-scale transport processes are abstracted into a large-scale view of the system. Identical repetitive elements are mapped onto one representative period, which simplifies the analysis significantly. The power of Macroransport Theory is its ability to easily obtain the average velocity and dispersion of groups of molecules without considering small scale details of molecular motion and interaction in the sieving media.

In his PhD thesis, Dorfman created a discrete macrotransport framework to analyze the velocity and dispersion of molecules in periodic microfluidic separation devices[31]. Furthermore, Dorfman et al. created a model for large (10-100 kbp) DNA moving through a nanofilter array identical to the one used in our experiments[32]. In this model, the amount of time it took the DNA to cross each trap, the trapping time, is converted into an effective additional distance to travel. The results of this model, for which the trapping time was extracted from experimental data, matched the experimental results qualitatively but not quantitatively.

In this section, we develop a macrotransport model for small (10-1000 bp) DNA moving through a nanofilter array. We begin by mapping each deep region and half of each adjacent shallow region of our periodic nanofilter array to a state. Molecules that move within a period do not contribute to a state transition: only molecules that cross the threshold between periods transition states. One assumption of this model is that once a molecule enters a deep region (a single state), dispersion within that 'state' (within a deep region) is fast (either by field-driven convection or diffusion) compared to the transitions between states. In such a 'perfect' mixing case, one could conceptually ignore any complex 3D convection and dispersion within a deep region, therefore significantly diminishing the complexity of the problem at hand.

Molecules in a state (a deep region) can move to an adjacent deep region. This movement is classified as a transition between the two neighboring states. These transitions are initiated by electrophoresis and diffusion, Figure 4.1. By characterizing transitions out of a one particular state for some class of molecules, we can make generalizations about the macroscopic behavior of this class.

For this model, we assume DNA free solution mobility is independent of size. This assumption is generally valid for DNA larger than 400 bp, and is valid within 5% from 400 bp down to 100 bp[33]. We assume that this free solution mobility and diffusivity is the same in the shallow region and the deep region, although the diffusivity of DNA located between parallel plates is known to be somewhat less than its diffusivity in free solution[34]. Additionally, it is arguable, although conclusive evidence is not available, that the electrophoretic mobility of DNA in the size range of interest is different in a parallel plate microchannel[35]. Even in that study, 1-15 kbp DNA electrophoretic mobility differed by approximately 7% over the entire range. We do not consider the dipole-inducing orientation effects of the electric field on the DNA partitioning between shallow and deep regions[36]. Despite these simplifications, the results of our model agree reasonably well with experimental results.

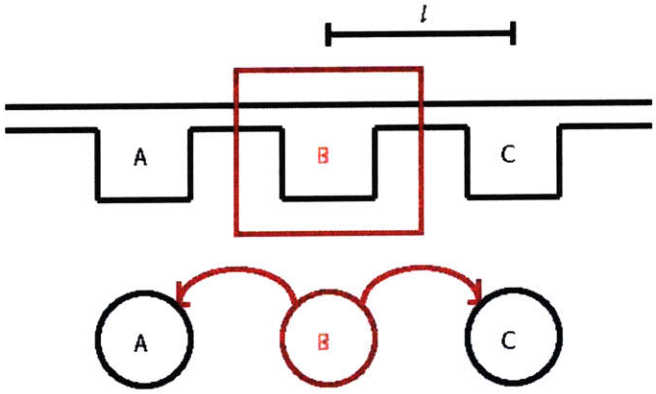

Figure 4.1: Mapping of each nanofilter period into a state.

We start by defining variables. Variables with a subscript n are dependent on DNA size.

x ≡ position
V ≡ period volume
l ≡ period length
A ≡ cross-section area through which molecule transitions between periods
d_s ≡ depth of shallow region
d_d ≡ depth of deep region
a ≡ d_d/d_s
t_o ≡ duration of time
U ≡ velocity of DNA in the ***shallow*** region
D_n ≡ diffusion coefficient
P_n ≡ concentration of molecules at A relative to overall concentration in V
L ≡ distance from separation region entrance to observation point
$t_{n,travel}$ ≡ mean elution time for a group of molecules

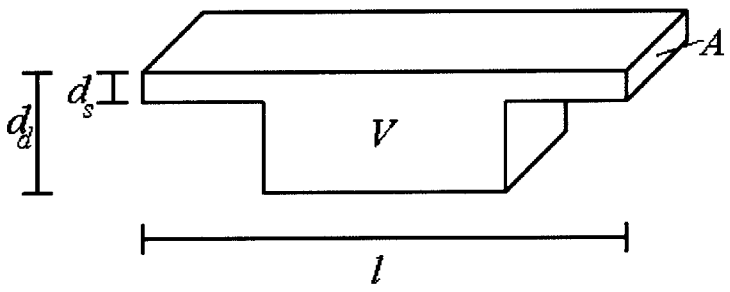

Figure 4.2: Dimensional variables with respect to nanofilter period. V refers to the entire volume of the period. The out-of-page dimension is not to scale: it is much larger than the other two dimensions.

Time is partitioned into very small discrete segments of duration t_o. The velocity of DNA in the shallow region, U, is independent of DNA size. We arbitrarily make convective velocity point to the right. To determine U, we first extrapolate the time it takes for a point-sized particle to elute, as mentioned in the Materials and Methods chapter. Theoretically, the velocity of point-sized particles is not affected by the constrictions: their movement only depends on electric field. The electric field in the deep region is $1/a$ its value in the shallow region, using Gauss' Law. The velocity of the point particle in the deep region is then U/a, assuming mobility is independent of electric field. The overall velocity is then:

$$\frac{L}{time_{point,travel}} = \frac{l}{\frac{l}{2U} + \frac{la}{2U}}$$

$$U = \frac{a+1}{2}\frac{L}{time_{point,travel}}$$

To calculate P_n, we use the concept of a partition coefficient, which is the relative concentration of molecules in a constrained region relative to a free region. The partition coefficient for rigid rods between parallel plates separated by distance d is given by[37]

$$K = 1 - \frac{1}{2}\frac{l_{rod}}{d} \qquad \text{when } \frac{l_{rod}}{d} \le 1$$

$$K = \frac{1}{2}\frac{d}{l_{rod}} \qquad \text{otherwise}$$

We approximate the DNA molecules as semi-rigid rods, following the Kratky-Porod worm-like chain model[38]. The equation relating the DNA size to the end-to-end length is

$$L = \left(2l_n l_p\left(1 - \frac{l_p}{l_n}\left(1 - \exp(-\frac{l_n}{l_p})\right)\right)\right)^{1/2}$$

where l_p is the persistence length and l_n is the contour length of the DNA. A typical value of l_p is 50 nm, which corresponds to 147 bp. The contour length l_n is the size in bp, n, multiplied by the rise per base pair, 0.34 nm/bp.

Modeling the DNA as rods, we first determine the available volume for DNA in the shallow region, using C as a reference concentration.

$$C_{shallow} = K_{shallow} C$$

The overall concentration in the entire period is the number of molecules in the shallow and deep regions divided by the overall volume:

$$C_{overall} = \frac{K_{shallow} C V_{shallow} + K_{deep} C V_{deep}}{V_{shallow} + V_{deep}}$$

then

$$P_n = \frac{C_{shallow}}{C_{overall}} = \frac{K_{shallow}\left(V_{shallow} + V_{deep}\right)}{K_{shallow} V_{shallow} + K_{deep} V_{deep}}$$

First we consider electrophoresis-driven movement. In one time step, the proportion of molecules transitioning out of a state is

$$\frac{t_o (P_n A U)}{V}$$

where the expression in parenthesis is the flux out of the period.

In diffusion-driven movement, the diffusive velocity is defined as

$$\frac{D_n}{l}$$

Analogous to electrophoresis-driven movement, the proportion of molecules transitioning out of a state by diffusion-driven movement is

$$\frac{t_o (P_n A D_n)}{V l}$$

The average velocity of the molecules is the expected value of the molecules' position after one time step, divided by the duration of one time step:

$$V_n = \frac{E[x]}{t_o}$$
$$= \frac{\left(\frac{t_o(P_nAU)}{V} + \frac{t_o(P_nAD_n)}{Vl}\right)l - \frac{t_o(P_nAD_n)}{Vl}l}{t_o}$$
$$= \frac{P_nAU}{V}l$$

The variance of the molecule's position after time t_0 is

$$E[(x-\bar{x})^2] = \left(\frac{t_o(P_nAU)}{V} + \frac{t_o(P_nAD_n)}{Vl}\right)l^2 + \frac{t_o(P_nAD_n)}{Vl}l^2 - \left(\frac{t_o(P_nAU)}{V}l\right)^2$$

As we partition time finer and finer, the last term in the expression becomes insignificant, relative to the first two terms:

$$\lim_{t_0 \to 0} E[(x-\bar{x})^2] \cong \left(\frac{t_o(P_nAU)}{V} + \frac{t_o(P_nAD_n)}{Vl}\right)l^2 + \frac{t_o(P_nAD_n)}{Vl}l^2$$

The effective diffusivity is then defined as

$$D^* = \frac{1}{2}\frac{d}{dt}E[(x-\bar{x})^2]$$
$$= \frac{1}{2}\frac{P_nA}{V}\left(U + 2\frac{D_n}{l}\right)l^2$$

To approximate the standard deviation of the species electropherogram at the point of observation, we calculate the SD in distance and then convert it into the SD in time by dividing by the empirical velocity.

$$SD_{n,distance} = \sqrt{2D^* t_{n,travel}}$$
$$= \sqrt{\frac{P_nA}{V}\left(U + 2\frac{D_n}{l}\right)l^2 t_{n,travel}}$$
$$SD_{n,time} \cong \frac{SD_{n,distance}t_{n,travel}}{L}$$
$$= \sqrt{\frac{P_nA}{V}\left(U + 2\frac{D_n}{l}\right)l^2 t_{n,travel}}\,\frac{t_{n,travel}}{L}$$

Diffusion Constant Modification to Incorporate Convective Band Spreading in Shallow Region

The diffusion constant that we used above D_n only accounts for pure molecular diffusion across nanofilters. A more accurate description takes into account the spreading due to the electric field strength and contours in the shallow region: if molecular diffusion were negligible with respect to axial velocity in the shallow region, molecules would still spread in a racetrack-like way, Figure 4.3.

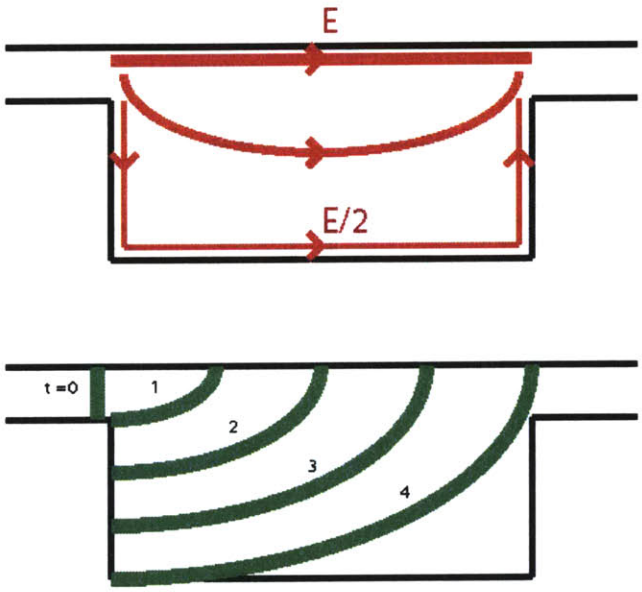

Figure 4.3: Top: Representative average electric field lines and strengths. The average field strength along the bottom and sides of the deep region is half that along the top, if the length of the deep region is twice its depth. This conclusion follows from unique voltages at the entrance and exit of the deep region, and the lengths of the bottom and sides being approximately twice that of the top. Bottom: DNA plug spreading due to differences in electric field strength. A molecule moving along the top edge will arrive at the exit in ¼ the time of a molecule traveling along the sides and bottom, since the electric field strength is half as strong and the contour length is twice as large for the sides and bottom compared to the top.

We can model this convective spreading in a similar manner as band spreading in a microfluidic channel turn. As an approximation, we map our rectangular geometry onto a semicircle turn geometry by equating the inner semicircle length to the top deep region length, and the outer semicircle length to the sum of the lengths of the sides and bottom. From Griffiths and Nilson[39], an effective diffusion constant for the spreading in a turn is

$$D_{eff} = \frac{U^2 a^4 \theta}{30 r^2 D\theta + 6Ua^2 r} + D$$

where U is the average flow speed, a is the channel width, θ is the angle of the turn, r is the average radius, and D is the molecular diffusivity.

In the context of our 80/320 nm devices, $(D_{eff}-D)/D$ was on the order of 10^{-3}: the racetrack effect is not significant. The values we use for this calculation are U = 10^{-3} cm/s (the fastest velocity in our experiments), a = (320*2+500-500)/π = 1.8×10^{-5} cm, θ = π, r = (320*2+500+500)/(2π) = 2.1×10^{-5} cm, and D = 10^{-7} cm^2/s. As a result, $D_{eff} = 7.9*10^{-11} + D$.

Intuitively, we can rationalize why this is the case by examining the Peclet number. To calculate the Peclet number, which describes the ratio between convective and diffusive velocity, we use 10^{-3} cm^2/s

as the convective velocity in the deep region, 10^{-7} cm^2/s as D and 320×10^{-7} cm as the depth of the deep region. Then Pe = .32, which indicates that in the time for the molecules to travel axially across a trap, the transverse concentration is smoothed out. Molecules in the faster streamline have time to diffuse into slower streamlines before traversing a period.

The racetrack effect could be important in devices with deeper deep regions, which would result in a larger Peclet number. From the equation above, a would increase, making the racetrack term more important. The reasoning is that the diffusion velocity would decrease dramatically, resulting in molecules having less time to move from one streamline to another.

Alternate Method of Deriving Dispersion due to State Residence Time Distribution

We make three assumptions:

1) Mapping of one period of the nanofilter array onto one state (i.e. what happens in one period does not affect what happens in the next)
2) Fast mixing within each period (or state) with respect to transition rate
3) Only transitions forward permitted (we only consider electrophoresis here)

We will discuss the validity of these assumptions later.

If the elapsed residence time of molecules in each state have no bearing on their time to transition, then the time to transition necessarily takes the form of an exponential. We use the same definitions as earlier and the new variable

$n \equiv L/l$ = number of states from start to detector

The expected time to transition for molecules in each state is

E[transition time] = $t_{n,travel}/n$

Based on the properties of the exponential probability density function, the variance of the time to transition is

$$\text{var(transition time)} = \text{E[transition time]}^2 = \left(\frac{t_{n,travel}}{n}\right)^2$$

Then the variance in elution time due to state residence is

var(elution time) = n*var(transition time)

The standard deviation in elution time is then

$$\text{SD(elution time)} = \frac{t_{n,travel}}{\sqrt{n}}$$

This expression is consistent with the earlier result, with D_n set to 0.

Assumption 1 implies that the residence time in one state has no effect on the residence time in the next state. In the context of our experiments, if molecular diffusion is completely absent, a molecule

would move along a given electric field line. Because some electric fields are stronger than others, molecules located on the higher electric field would consistently travel faster, filter after filter.

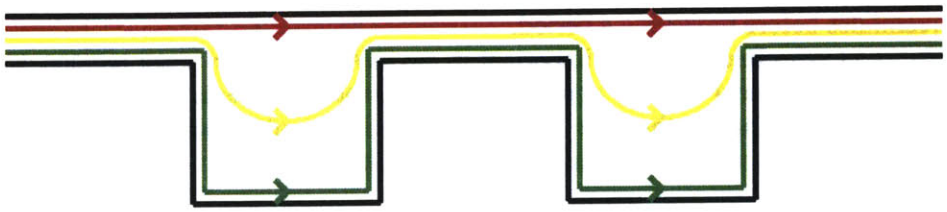

Figure 4.4: Electric field lines across two traps. The red electric field line is greater in magnitude than the yellow, which is greater than the green by uniqueness of potential. Then a molecule traveling on the red electric field line would travel much faster than a molecule on the green.

However, correlated speed across traps is not the case. A typical shallow region depth is on the order of 100 nm = 10^{-5} cm. Typical diffusivity values for DNA 100 – 1000 bp is 10^{-7} cm^2/s. Then a typical time constant for diffusion across streamlines in the shallow region is $l^2/D = 10^{-3}$ s. The time constant for crossing the shallow region is on the order of elution time / number of filters = 1000 s / 10^4 filters = 10^{-1} s / filter. Because the time constant for diffusion is much less than that for convection (i.e. the Peclet number << 1), many shallow region diffusion events can happen before a trap crossing. Hence the correlation in residence time in two consecutive traps due to staying on a field line is extinguished.

Assumption 2 implies that the concentration in the deep region is effectively uniform. If diffusion acts much faster than electrophoresis in the deep region, this assumption would be valid. The width of the deep region is 500 nm in all of our experiments. Using 10^{-7} cm^2/s as D, a typical time constant for diffusing across the deep region is on the order of 10^{-2} s. The time constant for crossing the deep region is on the order of 10^{-1} s. The diffusion time is approximately an order of magnitude less than the convection time. Therefore, the quick mixing assumption is generally valid.

Assumption 3 states that only forward movement is permitted. In our experiments, movement is caused by a combination of electrophoresis and electroosmosis. The electric field lines are derived from the electric potential, which satisfies Laplace's equation inside the channel. Furthermore, the electric field lines have no perpendicular component with respect to the walls (assuming uncharged walls). For electroosmotic flow at high buffer concentration, the flow profile is plug-like and effectively allows slip very close to the wall. The flow profile can be computed from a stream function, which again obeys Laplace's equation. Furthermore no fluid streamlines can be perpendicular to a wall. Because solutions to Laplace's equation with set boundary conditions are unique, the solutions to the electric potential and stream function are identical. Thus the electric field lines and fluid streamlines point in the same direction, with the ratio of their magnitudes being constant. From this analysis, there are no locations where electroosmotic flow overcomes electrophoresis to make the DNA move backwards.

Chapter 5

Characterization of Electric Field Dependent Nanofilter Separation Resolution

In previous experimental studies, researchers have shown that separation resolution is lost when the driving electric field is too strong for both the entropic trapping[4] and Ogston-sieving regimes[12]. When we increase the electric field strength, molecules elute sooner and separation results are obtained faster, which is a favorable outcome. However, the separation resolution gets poorer with increasing field. Fu et al. measured and characterized the degradation in separation selectivity with increasing electric field[12], but it is not yet clear how the increased field will affect the dispersion of the bands. Potentially, less dispersion would result, since molecules spend less time in the device and therefore there have less time to diffuse. However, it is unclear whether the dispersion is purely caused by diffusion, considering the inherent barriers in the channel.

In this chapter we investigate the changes in separation resolution with increasing electric field strength. Specifically, we examine its effects on selectivity and dispersion, which directly affect resolution.

Experimental Setup

Please refer to the Materials and Methods chapter for generic information regarding the experiments. Table 5.1 summarizes experimental parameters specific to this set of experiments.
Table 5.2 lists the voltages applied to each reservoir for the three steps of the experiments.

Device Dimensions	
Shallow region depth (d_s)	80 nm
Deep region depth (d_d)	320 nm
Buffer solution	TBE 5× (133 mM)
DNA	New England Biolabs 100 bp ladder
Voltages	Custom made voltage box connected to Stanford Research Systems, Inc., High Voltage Power Supply, Model PS325/2500V-25W

Table 5.1: Experimental setup for investigating electric-field effects on separation.

	Reservoir # (See Figure 3.2 for reference)			
	1	2	3	4
Loading	0	0	20	0
Injection	0	0	0	20
Run	15	0	15	χ

Table 5.2: Voltage configurations. The voltages used to alter the electric field are given by χ, where χ = 25, 30, 35, 40, 45, and 50 in these experiments.

Results and Discussion

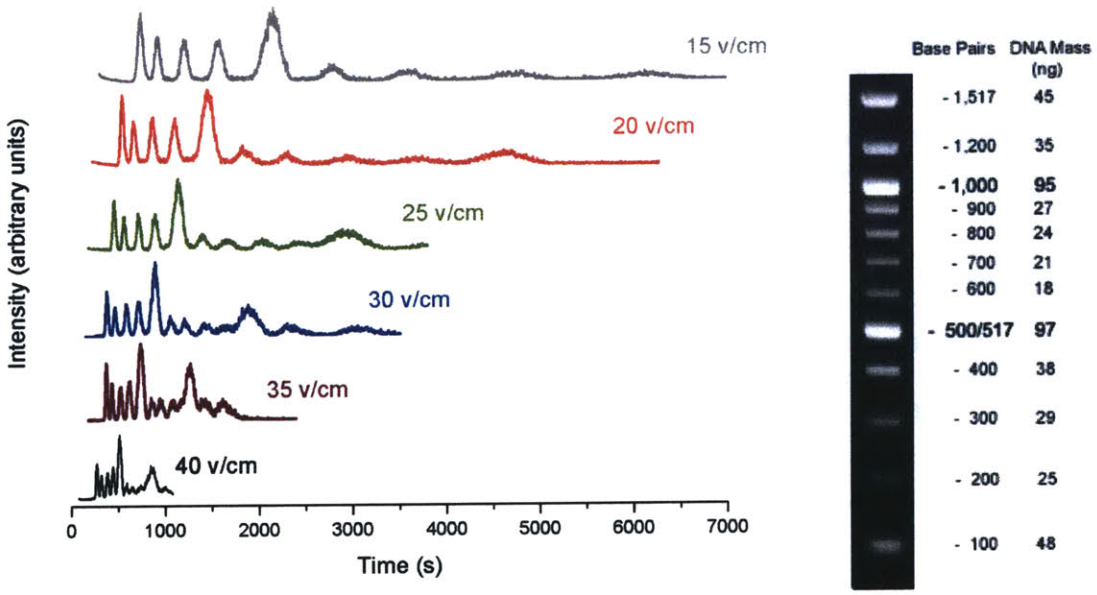

Figure 5.1: Left: Electropherograms illustrating the results obtained while altering the electric field. Note the convergence of the 500 to 1000 peaks as the field is increased, and hence the decrease in resolution. Additionally, note the faster elution times of all the peaks as the electric field is increased. Right: The manufacturer's specifications[40] of the DNA used.

According to the theory presented in Chapter 4, the velocity of the different DNA samples relative to an infinitesimally small DNA molecule is effectively given by the concentration ratio P_n. Also, the relative mobilities are independent of the applied voltage.

The theoretical predictions and experimental results match qualitatively. However, the model does not predict the differences in relative mobility for different E-fields. Furthermore, significant differences exist, especially for DNA greater than 500 bp, and the predicted relative mobilities are in the high range of experimental values, Figure 5.2.

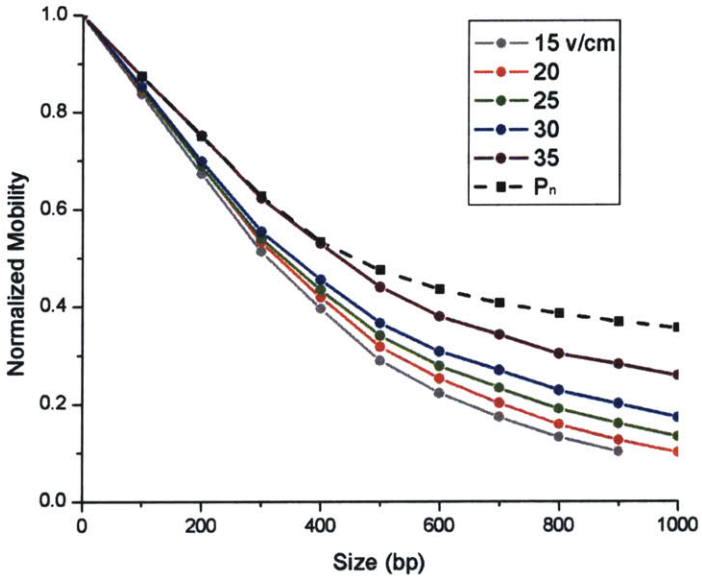

Figure 5.2: Normalized mobility vs. size for different electric fields. The predicted mobility is consistently at the top of the range of values.

As the electric field is increased, normalized DNA mobility in the entire size range increases. This increase is especially apparent for DNA larger than 500 bp. This increase in relative mobility may be caused by a reduction of the sieving properties of the constrictions: the higher electric field may be distorting the DNA shapes and forcefully dragging them through the constrictions. Less size-discrimination is the result.

Furthermore, the model, which is based on equilibrium partitioning models, may be limited in predicting the experimental results from an inherently dynamic (non-equilibrium) system. While it has been well-established that such equilibrium partitioning (free volume) models for electrophoresis work well, at least in the limit of low electric field, such a model is inherently an approximation and will break down with increasing electric field. One can give a simple scaling argument by comparing the timescales of diffusion vs. drift within the deep region. For a field value of 8.3 V/cm, the diffusion time and the drift time within the deep region of the channel are roughly the same[1]*. At this point, the assumptions of Macrotransport Theory and the perfect mixing concept in particular start to fail.

---

[1]* The diffusivity of 1000 bp DNA is 7.45×10^{-8} cm^2/s, according to Stellwagen et al.[41] The "diffusion velocity" over 0.5 μm is then 14.9×10^{-4} cm/s. The free solution mobility of DNA is 4.5×10^{-4} cm/s × cm/V, according to Stellwagen et al.[33] For the two velocities to be equal, the electric field would be 3.3 V/cm in the deep region. Assuming a 1 to 4 ratio of shallow region depth to deep region depth, the electric field would be 13.2 V/cm in the shallow region. Assuming a 1:1 shallow region length to deep region length, the overall electric field would be 8.3 V/cm.

The relative mobility deviations for DNA greater than 500 bp can be partially explained by the assumptions of the model. DNA was modeled as zero-diameter rods, whose length is determined by the end-to-end distance derived from the Kratky-Porod worm-like chain model[38]. The end-to-end length increases sub-linearly with respect to the DNA contour length, so the rod diameter must grow. For this reason, the partition coefficients for the longer DNA may be slightly inaccurate. A smaller partition coefficient would result from a cylinder instead of rod model. Furthermore, the rods are modeled as rigid. In practice, however, DNA with a contour length much greater than the persistence length is flexible. Such flexibility will create an additional degree of freedom (e.g. conformational), which should be considered to fully account for medium-sized DNA molecules.

More recently, Fu et al. demonstrated much better fitting using a model that separates the transit time from the trapping time[41]. The advantage of this theoretical model over Fu et al.'s model is the ability of this macrotransport model to systematically model dispersion, at least to a first order approximation. Since one of the primary goals of this work is to determine a model to analyze the dispersion behavior in the system, we will use this model from this point on.

Standard Deviation and Dispersion in the Nanofilter Array

The theoretical standard deviations are calculated using the experimental elution times and fastest velocities derived from experimental data. One assumption made in the theoretical standard deviation calculation is that the peak width at the start of the separation region is a delta: the peak has zero width. Impossible in practice, in our experiments the initial width is determined by the area of DNA we push into the channel and the 10 s concentration procedure. Furthermore, some leaking occurs from the sides of the injection T, as can be seen in Figure 7.3.

The injection T has a width of 40 μm, so a DNA profile of approximately this width goes into the separation region when we start the run. Because the period of our traps is 1 μm, this initial DNA movement into the traps covers approximately 40 traps.

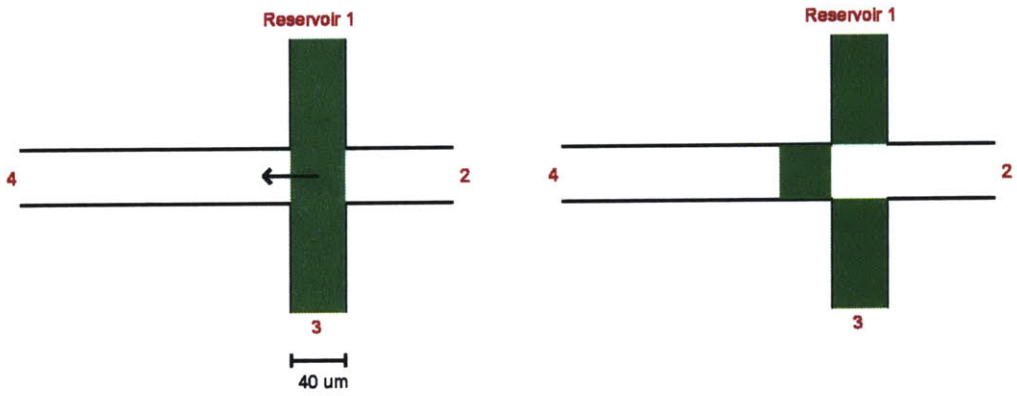

Figure 5.3: Illustration of the DNA plug's finite width being injected into the separation region.

The 10-second concentration time before each experiment, which was used to increase the fluorescence intensity level available for detection at the end of the channel, also increases the initial peak width. The elution time is on the order of 1000 s, and we used 5000 traps in this experiment. Then the velocity is on the order of 5 traps / s. Therefore, a 10 s load would inject molecules over approximately 50 traps.

Another effect is the leaking of DNA into the separation region upon application of separation voltage conditions, as can be seen in Figure 7.3. Overall, the initial peak width is far from zero: referring to Figure 7.3, the peak width is 200-250 traps. Although this figure was taken during experiments under

electrosmotic flow, the result is commonly seen in electrophoresis as well. From the data, the peak width at the detector location is 300-400 filters wide. Therefore, the initial peak width is non-negligible.

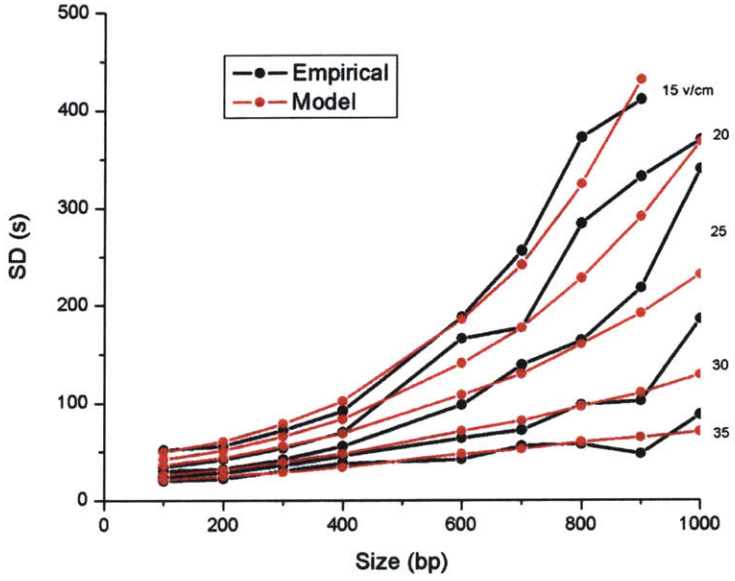

Figure 5.4: Empirical and theoretical standard deviations vs. size. To account for the finite launch width, we isolated the variance in position due to finite launch width for each data point by removing the diffusion and trap residence variance from the empirical variance. For each voltage condition, we averaged the finite launch width values and added this back to the theoretical diffusion and trap residence variance. We then convert this variance in distance to the standard deviation in time by taking the square root and dividing by the average velocity.

Resolution

The empirical resolution (in units of bp) was calculated from the elution time and standard deviation data:

$$R_{n+\frac{1}{2}} \equiv \frac{SD_{n+1,time} + SD_{n,time}}{t_{n+1,travel} - t_{n,travel}} \Delta size_{bp}$$

To calculate the theoretical resolution, only the velocity of an infinitesimally small DNA for each electric field was needed. All other parameters for the theoretical resolution were derived from this value, specifically the elution time and standard deviation.

The theoretical resolution is approximately 15-25 bp smaller than the empirical resolution in the range of 0-500 bp, Figure 5.5. This better predicted resolution is the result of assuming zero peak width at the start of separation. One important conclusion from the theory is that resolution can increase significantly by employing methods to decrease initial peak width.

In the range of 500-1000 bp, the theoretical resolution increases dramatically. This increase is a result of the theoretical normalized mobility being inaccurate, as explained earlier.

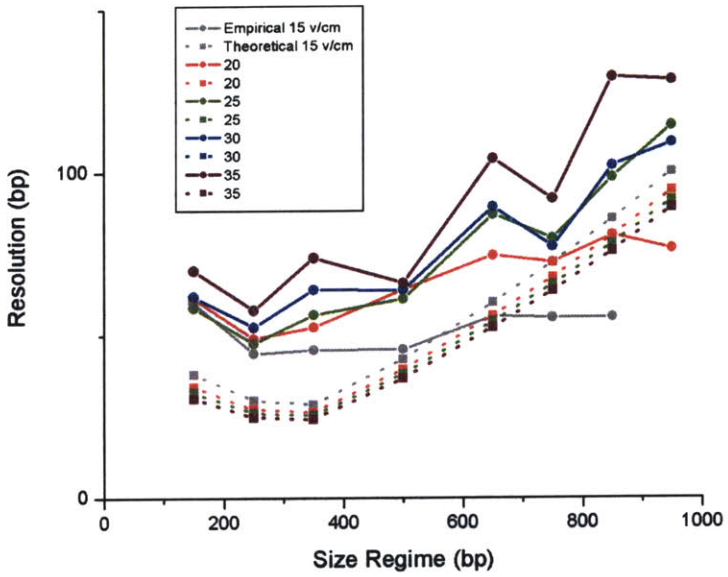

Figure 5.5: Empirical and theoretical resolution vs. size.

Conclusion

In this section we characterized the selectivity and dispersion of a nanofilter array device separating small DNA molecules. We applied a theoretical model based on Macrotransport Theory that roughly approximates these experimental results. The model predictions of normalized mobility match experimental data better for smaller-sized molecules. Since our goal is providing better separation for small biomolecules (such as proteins and carbohydrate) this model could provide useful insight.

Chapter 6

Characterization of Separation in Nanofilter Arrays with Different Structural Parameters

One of the qualities of regular nanofilter arrays for molecular separation is their precisely constructed pore size, compared to the random pore sizes in a gel. We hypothesized that changing the depth of the deep region would provide a tradeoff between separation resolution and separation speed. In the extreme limit of the deep region being the same depth as the shallow region, theoretically no separation would occur (no entropic energy barrier), but all of the molecules would elute quickly. When the deep region depth is only slightly greater than the shallow region depth, some separation would occur, but resolution would be poor. On the other extreme, when the deep region is extremely deep, molecules that enter would have very little probability of exiting, resulting in very long elution times but potentially great separation, due to large differences in molecular free volume. Similarly, the ability to separate molecules in nanofilter devices depends critically on the constriction at the entrance of the shallow region. Intuitively, as the constriction is made smaller, the selectivity will increase and the resolution will improve.

In this chapter, we characterize the separation resolution and selectivity in devices which differ in terms of shallow and deep region depths. Such characterization has been previously done for entropic trapping separation of long DNA polymers[42], but not for small molecule separation in the Ogston regime.

Experimental Setup

The following tables summarize the experimental setup and conditions.

Device Dimensions	
1. Shallow region depth: Deep region depth	60 nm: 480 nm
2. Shallow region depth: Deep region depth	60 nm: 240 nm
3. Shallow region depth: Deep region depth	80 nm: 320 nm
Buffer	TBE 5× (133 mM)
DNA	New England Biolabs PCR Marker Ladder
	New England Biolabs Low Molecular Weight Ladder
	New England Biolabs 100 bp Ladder

Table 6.1: Experimental setup for investigating the effect of structure parameters on separation.

In addition to the three devices used in these experiments, we fabricated two additional 60 nm thin region devices with deep regions of 120 and 960 nm and a 40/160 nm device. The 120 nm deep region device was created with 60 nm deep loading channels. Upon bonding the pyrex glass cover to the silicon wafer, these channels collapsed. Attempts to load fluid inside these channels were unsuccessful. The 960 nm deep region devices were structurally satisfactory, but filling the nanofilter region with TBE buffer consistently resulted in unfilled regions. Capillary forces and surface chemistry may have contributed to this difficulty with filling. Attempts to eliminate the bubbles using electroosmotic flow across reservoirs 2 and 4 were unsuccessful. A 40/160 nm device was created to further investigate the effect of the thin region depth on separation: This device failed to fill properly as well, as detailed in the Materials and Methods chapter.

	Reservoir			
	1	2	3	4
Loading	0	0	20	0
Injection	0	0	0	20
Run	15	0	15	χ

Table 6.2: Voltage configurations. The voltages used to alter the electric field are given by χ, where χ = 30, 35, and 40 in these experiments.

Results and Discussion

Deep region depth

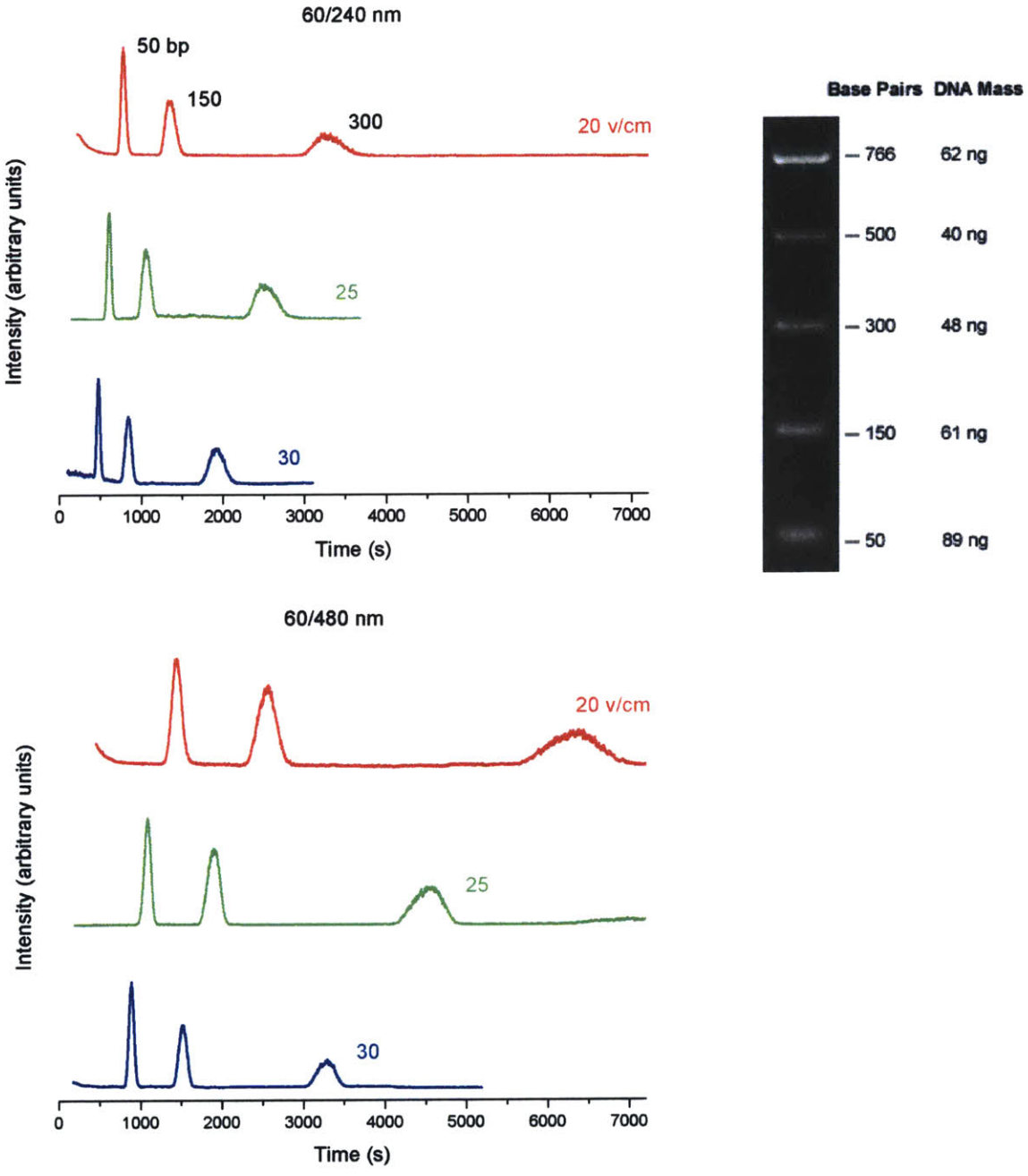

Figure 6.1: Top Left: Electropherograms illustrating the results obtained while altering the electric field in a 60/240 nm device. Only the 50, 150, and 300 bp peaks are shown. Right: The manufacturer's specifications for the PCR Marker Ladder used in these experiments[43]. Bottom Left: Electropherograms illustrating the results obtained while altering the electric field in a 60/480 nm device.

The elution times of respective samples at given potentials were greater in the 480 nm deep region device compared to the 240 deep region device by 1.83 ± 0.07 times, Figure 6.1. As illustrated in Figure 6.2, the electric field strength in the deep region is $1/a$ the value in the shallow region. In addition to the variables introduced in Chapter 4, we add the following variables:

E ≡ electric field in shallow region
V ≡ voltage drop across one nanofilter period
μ_0 ≡ mobility of point-size particle

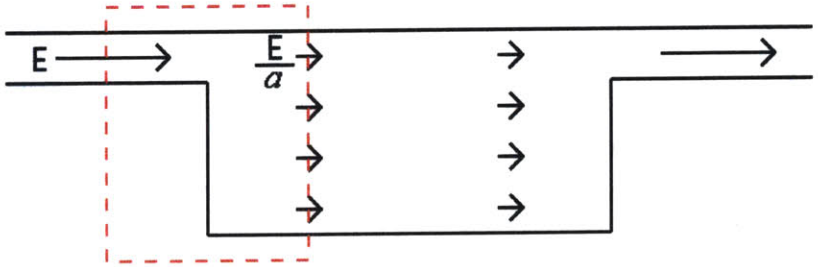

Figure 6.2: The electric field strength in the shallow region relative to the deep region is the same as the ratio in depths a, according to Gauss's Law. The red dashed rectangle is an example surface for application of this law.

$$\frac{E}{a}\frac{l}{2}+E\frac{l}{2}=V$$

$$E=\frac{2}{l}\frac{a}{a+1}V$$

$$\frac{L}{t_{point,travel}}=\frac{l/2}{\frac{a}{E\mu_o}l/2+\frac{1}{E\mu_o}l/2}$$

$$=\frac{E\mu_o}{a+1}$$

$$=\frac{a}{(a+1)^2}\frac{2}{l}V\mu_o$$

For the 60/240 and 60/480 nm devices used in these experiments, a is 4 and 8 respectively. Then the ratio of mobilities of a point-size particle should be 1.62. The observed mobilities for the 50, 150, and 300 bp samples differ by a constant value of approximately 1.83 ± 0.07 times, as mentioned earlier. This difference in mobility could be caused by the device dimensions deviating from the nominal dimensions or our assumption of constant electric field intensity with respect to depth.

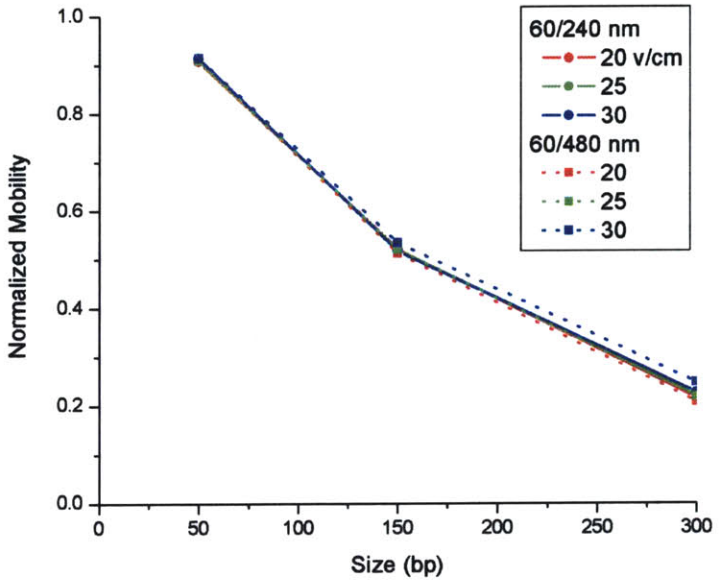

Figure 6.3: Comparison of normalized mobility between the two 60 nm shallow depth devices. The colors used are consistent with those used in Figure 6.1. To calculate the normalization constant, a linear least squares fit of the three points for each run was used. The normalized mobility slopes for the two devices are nearly identical: thus they have the same selectivity.

As seen in Figure 6.3, the normalized mobility plots for the two devices at all running voltage conditions are virtually identical: they differ by 2.0 ± 2.9% and at most 8.9% for the 300 bp sample. This statement is directly related to the constant ratio of elution times mentioned previously. From the nearly identical slopes of the normalized mobility plots, we conclude the sieving properties of the two devices are effectively the same.

Size (bp)	Normalized Mobility for 60/240 nm device	Normalized Mobility for 60/480 nm device	% difference
50	0.91	0.90	1.41
150	0.74	0.71	4.12
300	0.52	0.48	8.14

Table 6.3: Comparison of theoretical normalized mobility for 60/240 and 60/480 nm devices. The model used is presented in Chapter 3.

Although the theoretical results, Table 6.3, do not quantitatively match with the experimental results, Figure 6.3, the conclusion is the same: selectivity does not improve significantly for 60 nm shallow region devices when the deep region is increased past 240 nm.

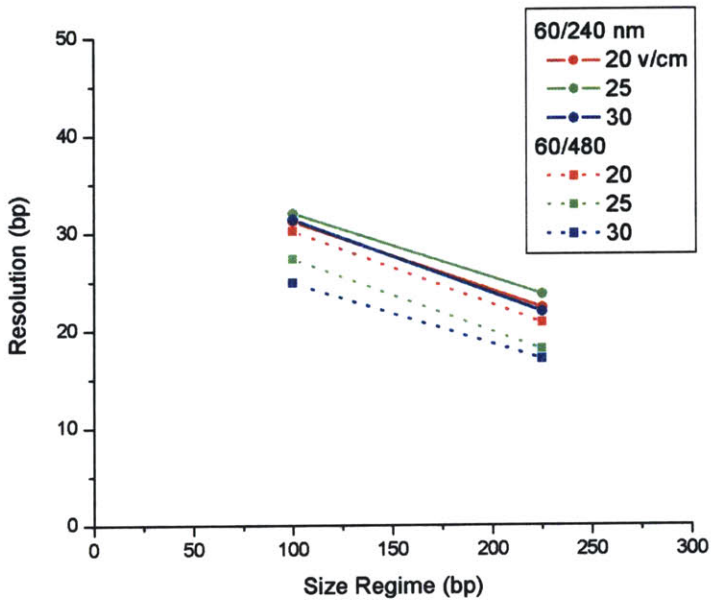

Figure 6.4: Comparison of resolution between the two 60 nm shallow depth devices. The colors are consistent with those used in Figure 6.1. The resolution of the 60/480 nm device is slightly better than that of the 60/240 nm device.

As can be observed in Figure 6.4, the 480 nm deep region device could resolve base-pair differences 4.02 ± 2.23 bp better than the 240 nm device, for a given electric field. This slight increase in resolving power could be associated with the decreased effective diffusivity for each sample: with a deeper deep region, the sample has less chance of finding the shallow region to escape. This decrease in dispersion, due to a lower effective diffusivity, makes the peaks modestly narrower for the 480 nm deep region device. A slightly better resolution is the result.

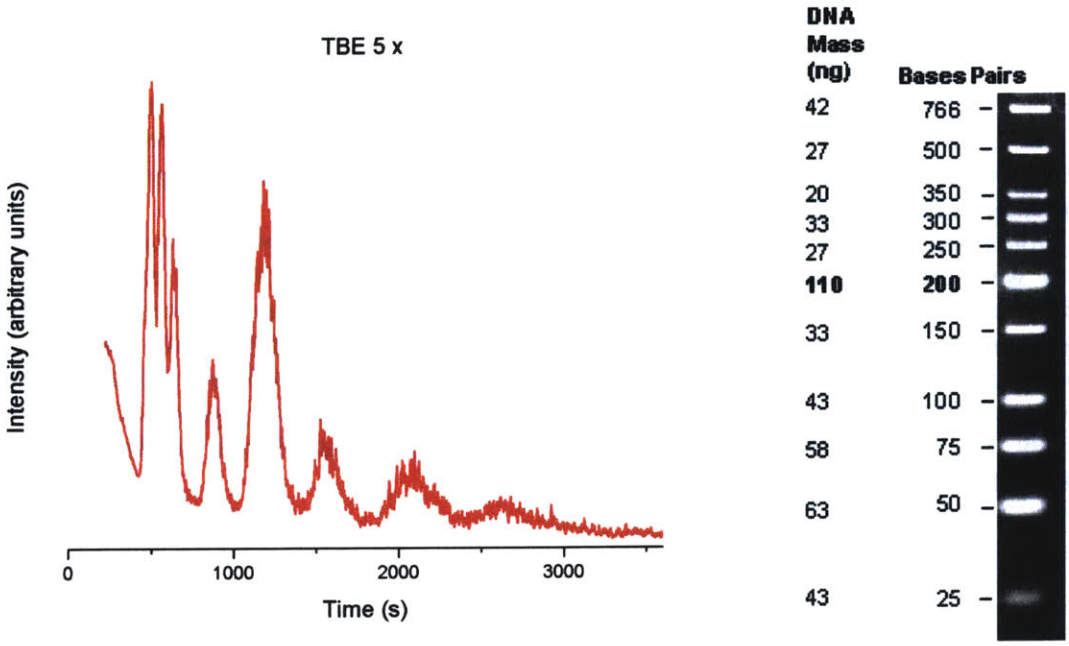

Figure 6.5: Left: Electropherogram illustrating the results obtained at 30 v/cm in a 60 nm shallow: 240 nm deep region depth device. Only the peaks up to 350 bp are shown. The 25 bp peak likely merged with the 50 bp peak. The decrease in fluorescence before 400 s is due to the laser intensity equilibrating. Right: The manufacturer's specifications for the Low Molecular Weight Ladder used in these experiments.

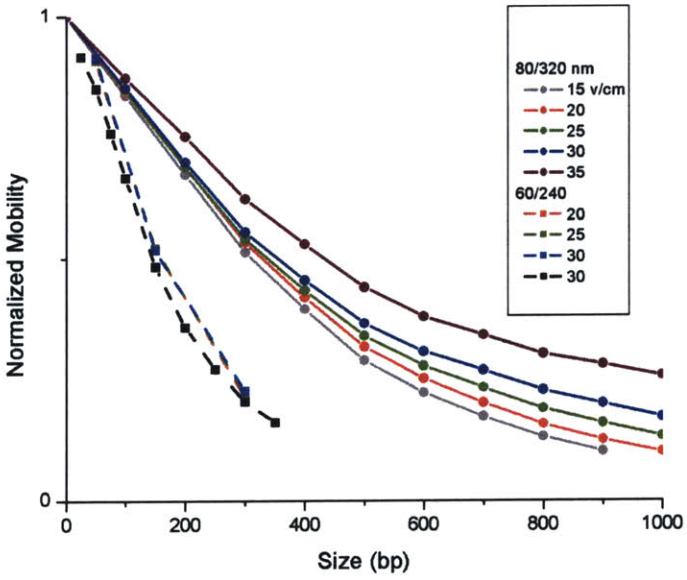

Figure 6.6: Normalized mobility vs. size for 80/320 and 60/240 nm devices. The data for the 80/320 nm device are extracted from Figure 5.1.

Shallow Region Depth with Fixed Ratio between Shallow and Deep

Because the ratio of deep region depth to shallow region depth was maintained in these two devices, the relative magnitude of the electric field in these two regions is also maintained. Theoretically, a point-size sample experiencing no sieving effects should elute from both devices at the same time, assuming the same voltage is applied. Thus differences of mean elution time and dispersion are due solely to the decrease in shallow region depth.

From Figure 6.6, the selectivity of the 60 nm device is substantially better than that of the 80 nm device. If we model the samples as semi-rigid rods, the relative mobilities in each case should be proportional to the partition coefficient in the shallow region. As a first-order approximation, the relative mobility should reach 0.5 when the length of the rod equals the depth of the shallow region. From the interpolated experimental results, 0.5 normalized mobility is reached for 300 bp and 180 bp DNA for the 80 and 60 nm shallow region devices, respectively. These DNA lengths correspond to 79.7 and 52.3 nm, respectively. The actual device shallow region dimensions are 80 nm and 60 nm, which show a qualitative agreement between the theoretical and experimental values.

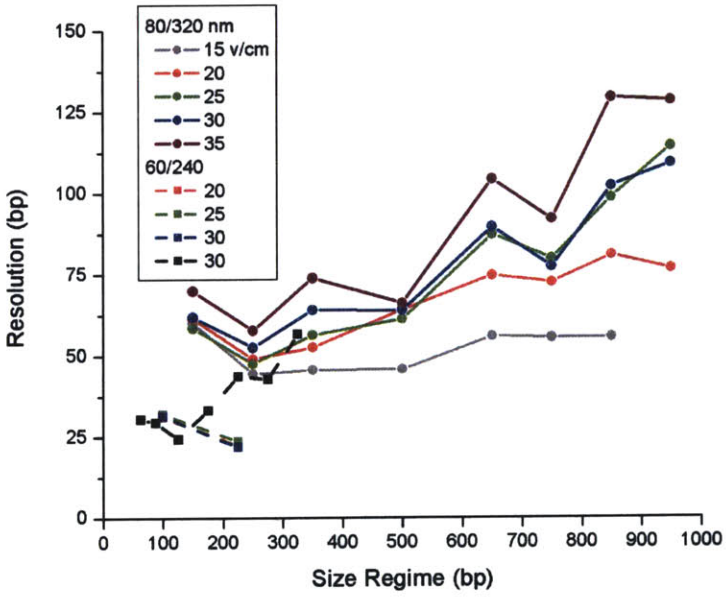

Figure 6.7: Resolution vs. size regime for the 80/320 and 60/240 nm devices.

From experiments, the 60 nm shallow region device could resolve differences of 30 bp for DNA smaller than 250 bp, while the 80 nm device could resolve differences of approximately 55 bp, Figure 6.7. According to the model, the reason for increased selectivity with smaller pores is the increased difference in steady state concentration in the shallow region versus the deep for molecules of different sizes. The dispersion observed in the electropherograms is mainly caused by the initial band width, as detailed in the previous chapter. Thus increased selectivity results in increased resolving power.

Conclusion

We have experimentally characterized the effect of changing the gap size of the nanofluidic filters on the separation resolution and speed. Increasing the deep region thickness makes the drift of the molecules in the deep region slower (due to 1/a factor), which leads to slower separation. However, there was no enhancement in selectivity by increasing the deep region depth, as expected from the model. Decreasing the shallow region depth significantly enhances the selectivity, because the partitioning of molecules between the deep and shallow regions is more extreme. In the next chapter, we will consider a method of making the pores smaller without altering the physical structure of the device.

Chapter 7

Control of Effective Nanofilter Gap Size by Ionic Strength

From the theoretical model, smaller pores should lead to increased size selectivity. Unfortunately, smaller pores are not always easy to make: filling problems commonly occurred for our devices with constrictions smaller than 50 nm. If we can make the effective pore size smaller, without altering the physical pore size, separation performance can be improved without as much difficulty.

Our devices are made of pyrex glass bonded to silicon dioxide, surfaces which carry an intrinsic negative charge. When the microfluidic channels are filled with buffer, DNA, which is also negatively charged, is repelled from the walls. The distance this repulsion is effective is on the order of the Debye length, which increases with decreasing buffer concentration. Furthermore, the zeta potential might increase with decreasing buffer concentration. These two effects may contribute to decrease the effective pore size, which is illustrated in Figure 7.1 . In this chapter, we test this hypothesis by experimentation using buffers of different ionic strengths.

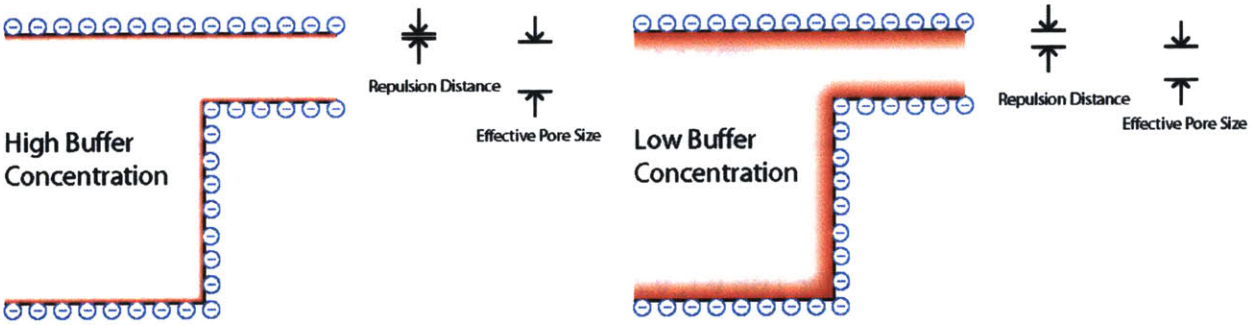

Figure 7.1: Illustration of effective pore size decrease by increasing the repulsion force a negatively charged particle feels from the walls. The red areas are those that the negatively charged particle has difficulty accessing.

Experimental setup

The general procedures described in Materials and Methods were followed for these experiments. Table 7.1 summarizes the experimental conditions. At buffer concentrations at and below TBE 1×, electroosmotic flow (EOF), instead of electrophoretic motion, dominated the direction of DNA movement. For this reason, the voltages used in these experiments are the negative of those used in TBE 5× experiments. The voltages used for the experiments are shown in Table 7.2 and Table 7.3; Figure 7.3 illustrates the loading, injection, and run at TBE 0.5× (44.5 mM).

Device Dimensions		
Shallow depth	80 nm	
Deep depth	330 nm	
Buffer	5× TBE	133 mM
	1×	26.6
	0.5×	13.3
	0.25×	6.65
	0.1×	2.66
DNA	New England Biolabs 100 bp ladder	

Table 7.1: Experimental conditions for investigating how buffer concentration affects selectivity.

	TBE 5× Reservoir			
	1	2	3	4
Loading	0	20	0	0
Injection	0	0	0	20
Run	0	-χ	0	χ

Table 7.2: Voltage configurations for TBE 5×. The voltages used to alter the electric field are given by χ, where χ = 5, 10, 15, and 20 in these experiments.

	TBE 0.1, 0.25, 0.5, 1× Reservoir			
	1	2	3	4
Loading	0	-20	0	0
Injection	0	0	0	-20
Run	0	χ	0	-χ

Table 7.3: Voltage configurations for TBE 0.1, 0.25, 0.5, and 1×. The voltages used to alter the electric field are given by χ, where χ = 20, 30, 40, and 50 in these experiments.

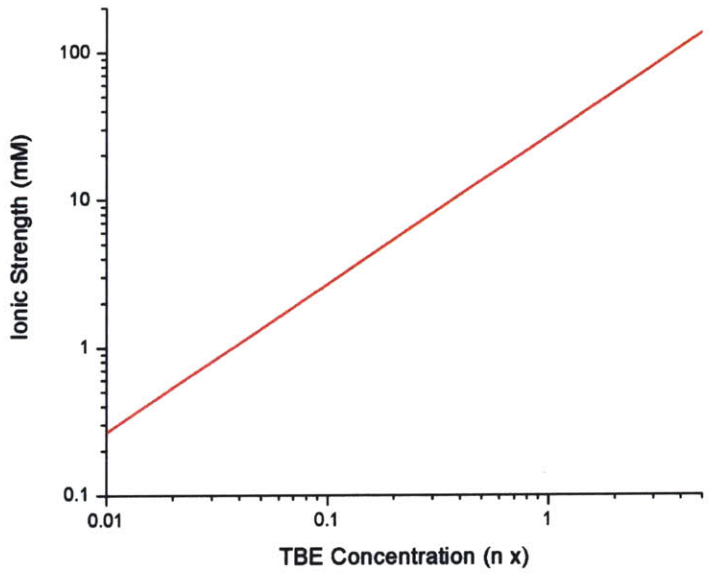

Figure 7.2: Ionic strength (mM) vs. TBE Concentration (n ×).

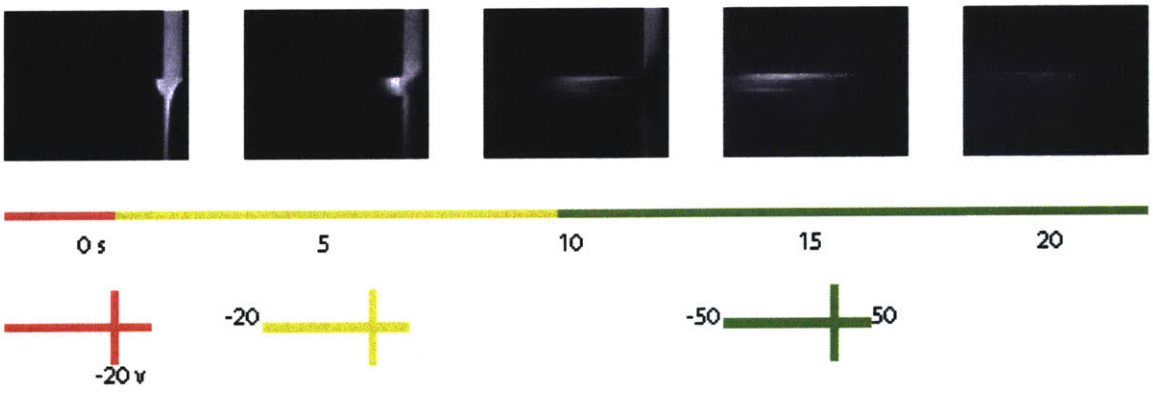

Figure 7.3: Representative loading, injection, and run at low TBE concentration. The experiment was done using TBE 0.5 ×. All channel widths are 40 μm. Thus at 15 seconds, the DNA profile looks to be 5-6 channel widths long, which corresponds to 200-240 μm, or 200-240 filters.

One issue encountered in these experiments is that even at relatively high electric fields (e.g. 100 v/cm), larger DNA molecules (> 1000 bp) took more than two hours to move through the nanofilter separation region. To expedite channel clearing, a 6-second periodic square wave alternating between 100 v/cm and 40 v/cm was used. This alternating electric field efficiently cleared the channel in less than 30 minutes. Instead of moving smoothly, the DNA jumped up to 10 nanofilters upon higher-field application, and moved back 2-3 nanofilters upon lower-field application. Relaxing the lower field to 0 v/cm did not work as well, since the DNA gave up almost all of its gains upon lower field application.

Results

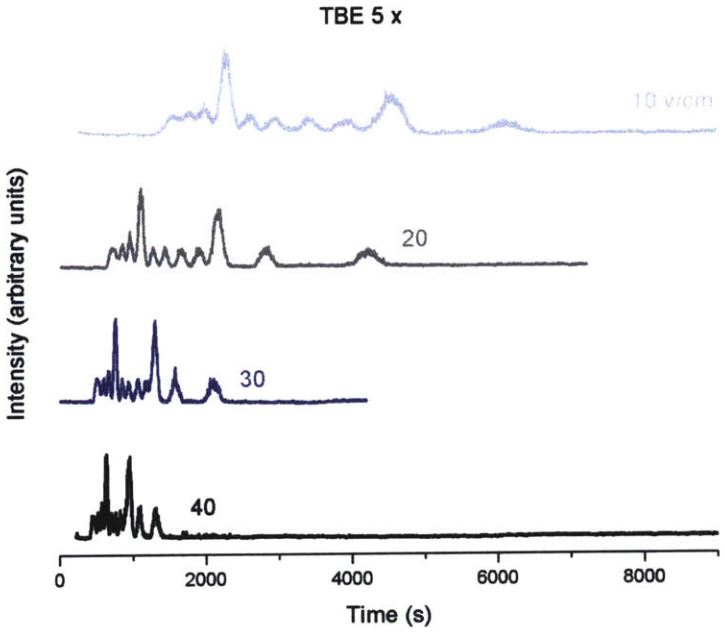
TBE 5 x
10 v/cm
20
30
40
Intensity (arbitrary units)
0
2000
4000
6000
8000
Time (s)

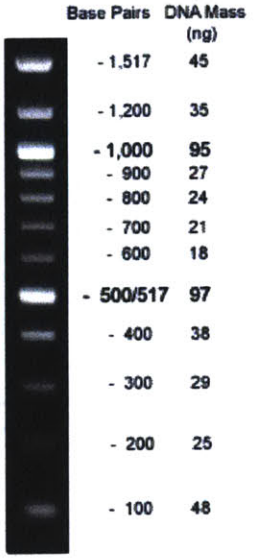
Base Pairs
DNA Mass (ng)
- 1,517 45
- 1,200 35
- 1,000 95
- 900 27
- 800 24
- 700 21
- 600 18
- 500/517 97
- 400 38
- 300 29
- 200 25
- 100 48

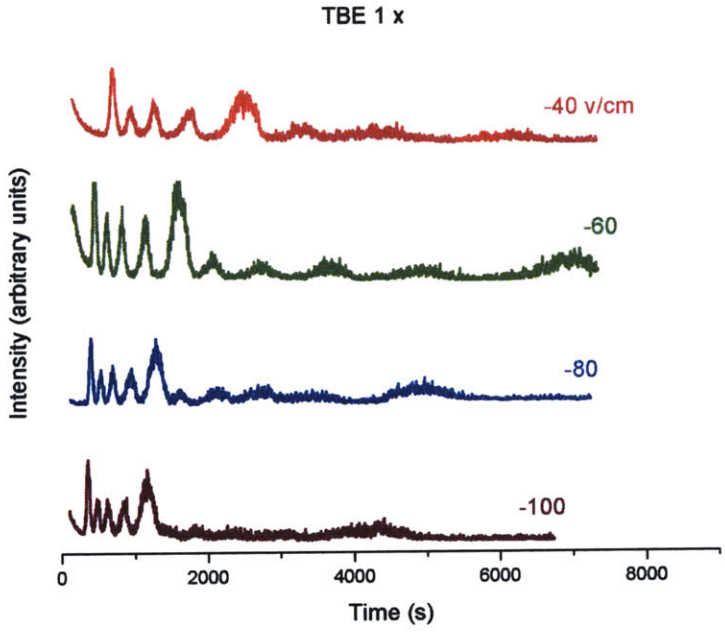
TBE 1 x
-40 v/cm
-60
-80
-100
Intensity (arbitrary units)
0
2000
4000
6000
8000
Time (s)

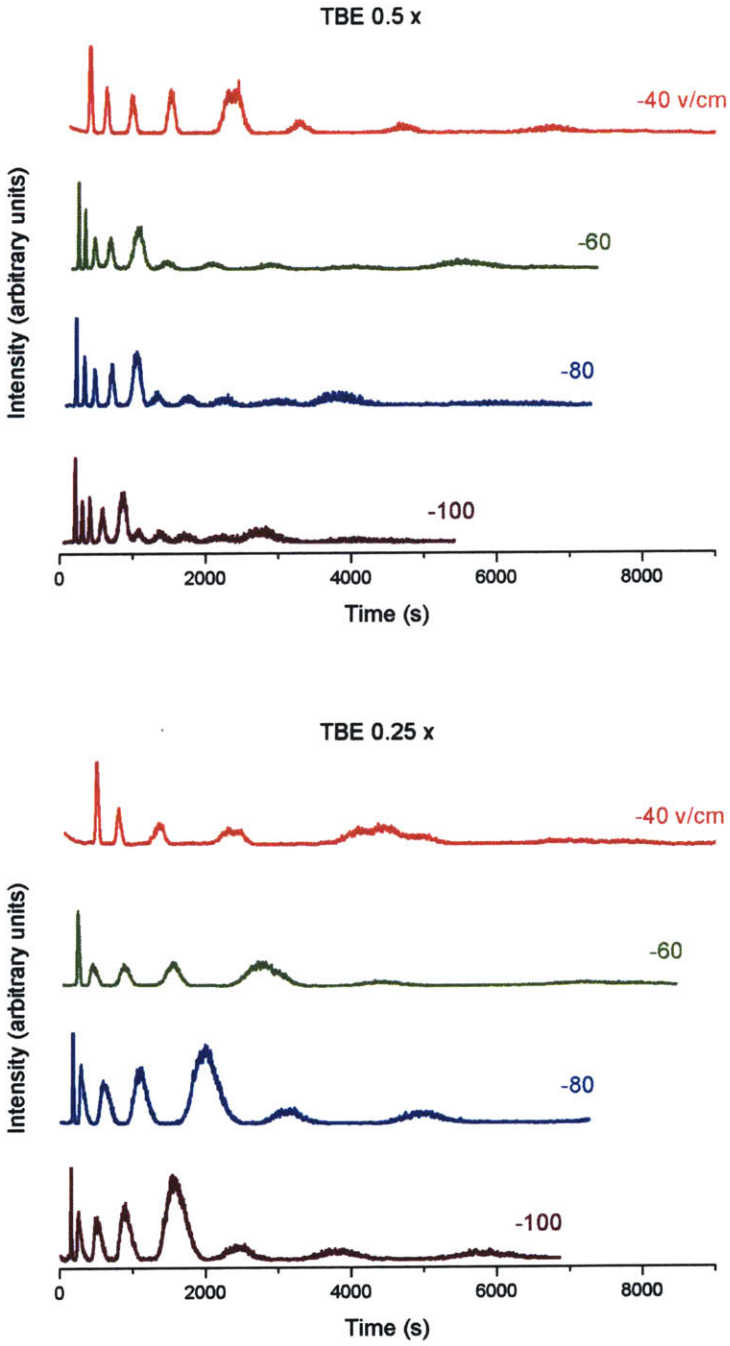

Figure 7.4: Electropherogram of results obtained with TBE 5, 1, 0.5, and 0.25×. Top Right: The manufacturer's specifications for the 100 bp Ladder used in these experiments[40].

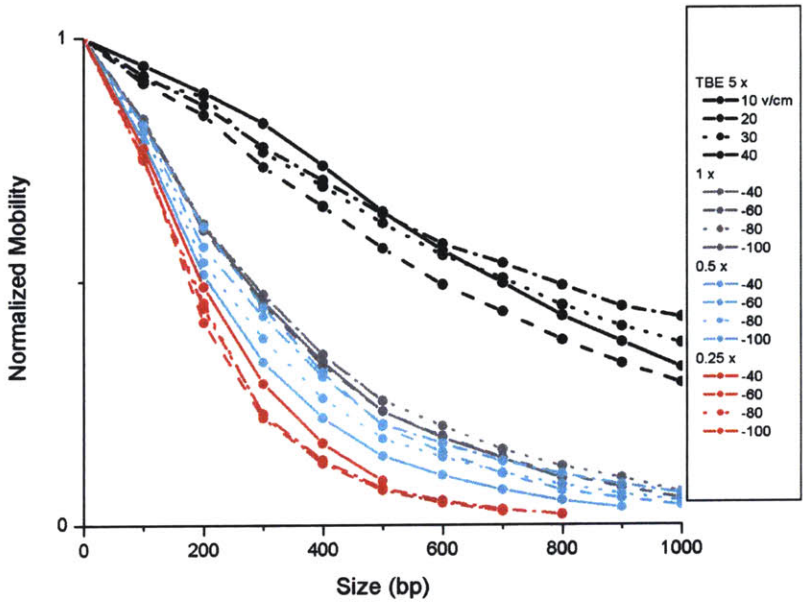

Figure 7.5: Normalized mobility vs. size for 0.25, 0.5, 1, and 5× TBE. The colors used in this figure do not match those used in previous figures. As the buffer concentration decreases, the normalized mobility slope becomes steeper, indicating increasing selectivity.

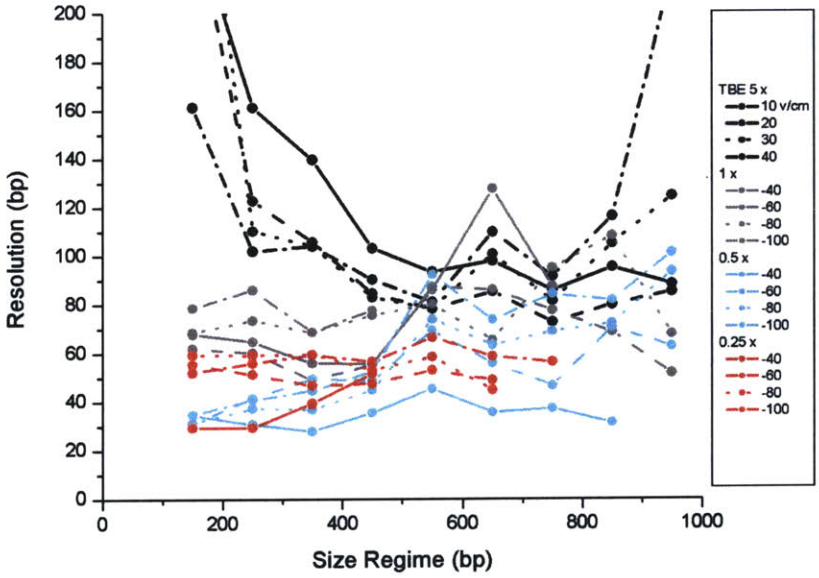

Figure 7.6: Resolution vs. size regime for different buffer concentrations and electric fields. The overall trend is that the selectivity, and therefore separation resolution, generally increased with lower buffer concentration.

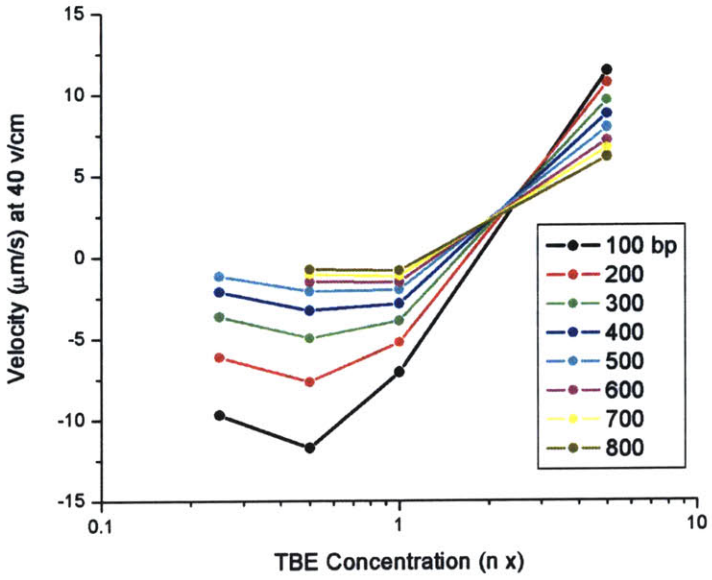

Figure 7.7: Velocity vs. buffer concentration. The DNA velocities reached a maximum negative value between 1 and 0.25× TBE. This effect may be explained by the additional sieving effects at even lower buffer concentrations, which results in lower absolute velocity for all of the DNA molecules. At the 0.25× TBE conditions, the Debye length is ~20nm, which is a significant portion of the nanochannel. This length could lead to a significantly non-plug-like flow profile, as well as a decrease in the electroosmotic flow velocity, as described by Rice and Whitehead[44].

Discussion

Electroosmotic Flow

When TBE of concentration less than 1× was used, the DNA moved in the same direction as electroosmotic flow. In the experiments using 5 × TBE, DNA motion was consistent with electrophoresis. To analyze DNA movement in the presence of these two forces, we focus on each one independently. We first provide a theoretical prediction of the TBE concentration when DNA has no net mobility in the presence of an electric field in our device. We then compare this prediction with our experimental findings.

Plug flow, with slip at the wall, adequately characterizes electroosmotic flow when the Debye length is much smaller than the characteristic cross-sectional dimension of the channel. For the buffer concentrations used in these experiments, the Debye lengths ranged from 0.8 nm to 3.8 nm, which is much smaller than the smallest channel dimension, 80 nm. As mentioned in the Background chapter, the fluid flow velocity can be approximated as plug-like with velocity given by

$$U = -\frac{\varepsilon \zeta E}{\mu}$$

The zeta potential for our experimental conditions can be approximated by[5]

$$\zeta = 0.0288 c^{-0.245}$$

where c represents ionic strength, measured in moles/liter; and ζ is the Zeta potential, in mV, Figure 7.8.

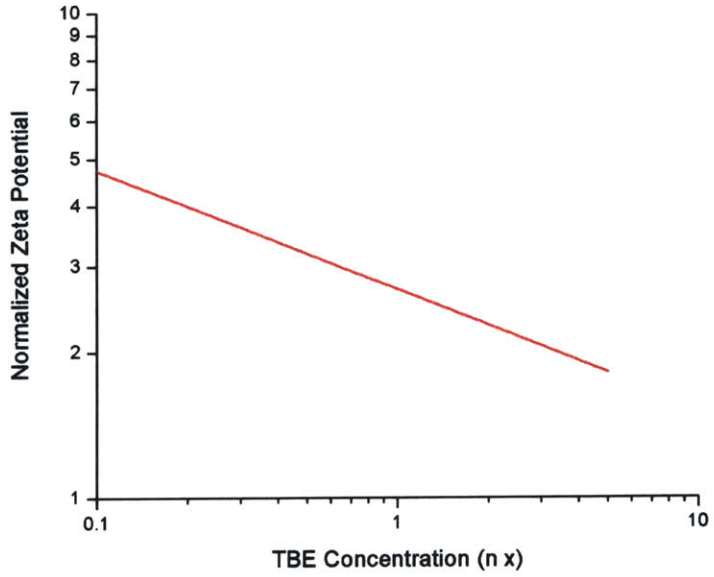

Figure 7.8: Normalized zeta potential vs. TBE concentration. The zeta potential is normalized to 26 mv, the voltage equivalent of thermal energy ($k_B T$).

DNA free solution mobilities range from 3.4 to 4.5 × 10^{-8} m^2/v·s for 0.2 to 2 × TBE, effectively independent of size[33, 45, 46]. We choose 4 × 10^{-8} m^2/v·s as a nominal value for DNA free solution mobility.

The net DNA velocity is a combination of electrophoresis and bulk electroosmotic flow.

$$v = -\mu_0 E + \frac{\varepsilon \zeta E}{\mu}$$

As both the electroosmotic flow velocity and electrophoretic velocity are proportional to the electric field, when we set magnitudes of the two velocities equal to each other we obtain a zeta potential value of 0.0568 V, or 2.18 normalized to 26 mV. This zeta potential corresponds to 2.5 × TBE. At this concentration, theoretically there will be no DNA movement. Above this concentration, the direction of DNA movement will be consistent with electrophoresis, and below this concentration movement will be consistent with electroosmosis.

In our experiments, we extrapolate 1.7× TBE will result in zero net DNA movement by linearly approximating the DNA velocity at 1 and 5× TBE, Figure 7.7. This experimental result is within a multiple of the theoretical result.

Selectivity and Ionic Strength

Although the depth of the shallow region is precisely defined by the fabrication processes, not all of it is easily accessible to negatively charged molecules due to electrostatic repulsion from the negatively charged walls. As defined in the background section, the concentration of a charged molecule with respect to electric potential can be approximated by the Boltzmann distribution.

$$c_i = c_{i\infty} \exp(\frac{-z_i F \phi}{RT})$$

where i represents the electric charge of the charged molecule. We define the accessible shallow region as the region where the electric potential becomes equal or less than the thermal voltage k_BT. The reasoning is that any energetic terms less than k_BT are insignificant compared to the thermal motion; therefore molecules are not repelled from the wall anymore in this region.

The potential at a distance x from the wall is given by

$$\phi = \zeta(c) \exp\left(-\frac{x}{\lambda_d(c)}\right)$$

where both the zeta potential and the debye length are functions of the buffer ionic strength. Figure 7.9 plots Debye length vs. TBE concentration, and Figure 7.10 shows the repulsion distance vs. TBE concentration. The repulsion distance is defined as the distance at which the electric potential drops to 26 mV.

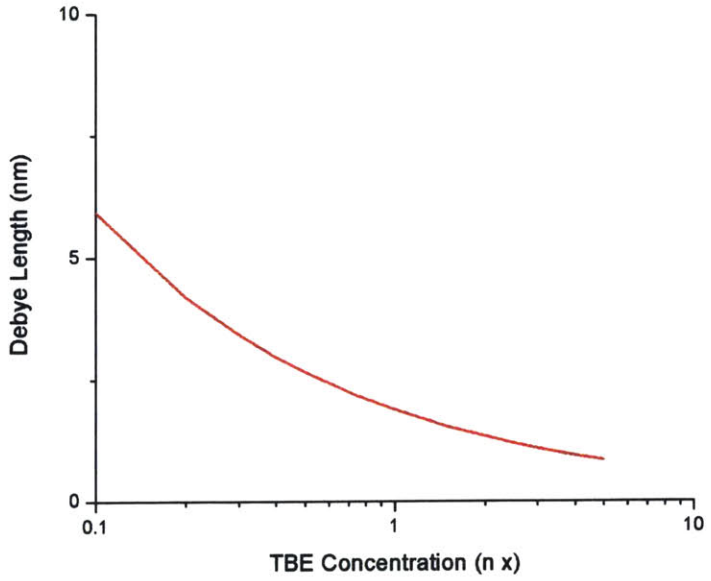

Figure 7.9: Debye length vs. TBE concentration

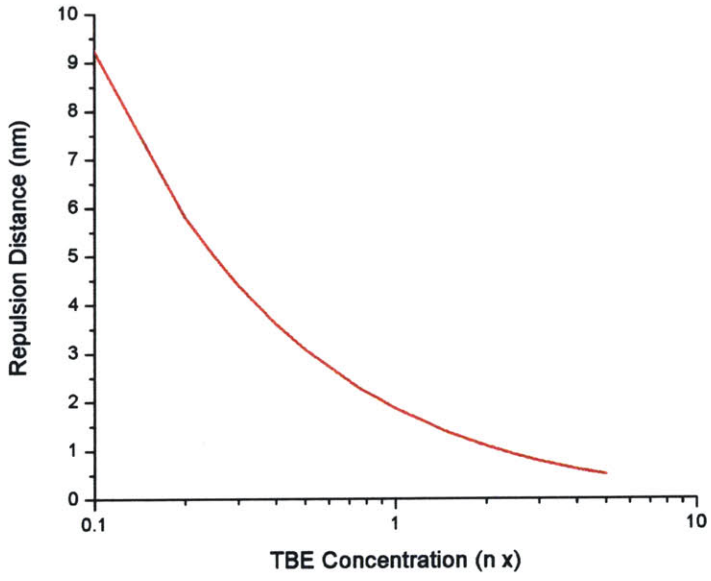

Figure 7.10: Repulsion distance vs. TBE concentration. The repulsion distance is defined as the distance from the wall at which the potential falls to 26 mV, the thermal voltage.

It is clear from Figure 7.10 that the repulsion distance for 5× TBE is on the order of 1 nm, which is insignificant compared to the 80 nm shallow region depth. The repulsion distance for 0.25× TBE is 5.0 nm. Because the shallow region consists of two walls, an effective gap size decrease of 10.0 nm is the result. Combined with an effective increase in DNA end-to-end length, due to the same phenomena, the selectivity of the 80 nm device run with 0.25 × TBE should be similar to that of the 60 nm device run with TBE 5 ×. Indeed, the results are similar, **Figure 7.11**.

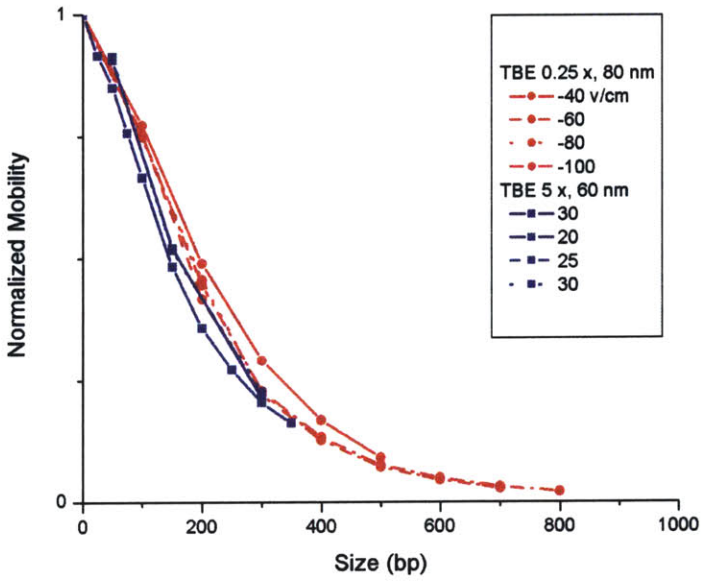

Figure 7.11: Normalized mobility vs. size of 80/320 nm device run with TBE 0.25× and 60/240 nm device run with TBE 5×.

Non-uniform Free Solution Mobility of Small DNA

DNA electrophoretic mobility is generally size-independent, with an exception in the regime of small DNA molecules. According to Stellwagen et al, the free solution mobility of DNA in TBE buffer increases monotonically from 0 to 400 bp and remains constant from 400 bp to 48.5 kbp [33]. In their experiments, the extrapolated mobility varied from 4.4 $cm^2V^{-1}s^{-1}$ for 100 bp to 4.5 x 10^4 $cm^2V^{-1}s^{-1}$ for 400 bp in TBE 0.5×; 400 bp DNA traveled 2.7% faster than 100 bp DNA. In these experiments, smaller DNA traveled slower. If DNA mobility increased with size, in electrophorsis-driven movement larger DNA would elute sooner. Conversely, in electroosmotic-driven movement smaller DNA would elute sooner. In our experiments, smaller DNA consistently elutes earlier. Thus running our experiments under electroosmotic-driven movement helps our separation result.

In our experiments, smaller DNA traveled faster regardless of buffer concentration. One relevant difference between the experimental setups is the presence of constrictions in our devices, which retards larger molecules more than smaller ones. In our electrophoresis experiments using 5× TBE, 100 bp DNA traveled 32.2 ± 14.9 % faster than 400 bp DNA. Additionally, in our 1 , 0.5, and 0.25 × TBE experiments, 100 bp DNA traveled 143 ± 64.6 %, 200 ± 97.5 %, 451 ± 209 % faster, respectively, than 400 bp DNA. Clearly, in our experiments the sieving effect of the constrictions is much more important than differences in free solution mobility.

Persistence Length Changes

One might also argue that the persistence length, which represents the stiffness of the DNA molecules, might be different at different buffer concentrations. In theory, DNA persistence length increases when buffer concentration decreases. This effect is caused by the decreased screening of electrostatic repulsion between neighboring molecules, which results in longer stretches oriented in the same direction. Longer persistence lengths lead to greater size differences, resulting in better selectivity.

However, this effect is not prominent in practice. For the ~1-100 mM ionic strengths investigated in our experiments, the persistence length ranged from 350 to 550 nm, with most results between 440 and 550 nm[47], with no observable correlation between persistence length and ionic strength.

Conclusion

We have successfully demonstrated the validity of our hypothesis, that decreasing buffer concentration leads to increased selectivity. This method of increasing selectivity could be a useful technique for separating smaller biomolecules such as small proteins and carbohydrates. Also, despite propulsion by electroosmotic flow, similar sieving behavior was observed. This demonstration suggests the possibility of running the separation system entirely using external pressure, enhancing separation speed and throughput.

Chapter 8

Conclusion

Our initial goal in conducting these studies was to find ways of increasing the resolution of microfabricated nanofilter devices for the purpose of separating even smaller molecules, such as carbohydrates. We have learned that increasing the electric field affects primarily larger molecules. A simple macrotransport model can be used for analyzing separation selectivity and dispersion. This model's predictions are consistent with experimental results. The deep region depth is much less important to separation resolution than the shallow region depth, although the shallow region depth is difficult to shrink. Additionally, we have concluded that lowering buffer concentration increases size-selectivity by decreasing the effective pore size.

With the knowledge gained from these studies, we plan on tackling the challenge of separating carbohydrates by first constructing devices we are able to fill with the smallest pores possible. The size of these pores will probably be around 45-50 nm. Then we will determine the lowest buffer concentration that allows molecules to enter the pores, but also increases the selectivity. In additional to conventional photolithography processes, we will also investigate increasing the number of nanofilters per unit length by using e-beam photolithography.

Bibliography

1. Senturia, S. D. Microsystem Design. (2001).
2. Dittrich, P. S., Tachikawa, K. & Manz, A. Micro Total Analysis Sytems. Latest Advancements and Trends. Analytical Chemistry (2006).
3. Chou, C.-F. et al. Sorting biomolecules with microdevices. Electrophoresis 21, 81-90 (2000).
4. Han, J. & Craighead, H. Separation of long DNA molecules in a microfabricated entropic trap array. Science 288, 1026-1029 (2000).
5. Pennathur, S. & Santiago, J. G. Electrokinetic Transport in Nanochannels. 2. Experiments. Analytical Chemistry 77, 6782-6789 (2005).
6. Macounova, K., Cabrera, C. & Yager, P. Concentration and separation of proteins in microfluidic channels on the basis of transverse IEF. Analytical Chemistry 73, 1627-1633 (2001).
7. Lakshmi, B. B. & Martin, C. R. Enantioseparation using apoenzymes immobilized in a porous polymeric membrane. Nature 388, 758-760 (1997).
8. van Oudenaarden, A. & Boxer, S. G. Brownian ratchets: molecular separations in lipid bilayers supported on patterned arrays. Science 285, 1046-1048 (1999).
9. Huang, L. R., Cox, E. C., Austin, R. H. & Strum, J. C. Continuous particle separation through deterministic lateral displacement. Science 304, 987-990 (2004).
10. Huang, L. R. et al. A DNA prism for high-speed continuous fractionation of large DNA molecules. Nature Biotechnology 20, 1048-1051 (2002).
11. Fu, J., Mao, P. & Han, J. Nanofilter array chip for fast gel-free biomolecule separation. Applied Physics Letters 87, 263902 (2005).
12. Fu, J., Mao, P. & Han, J. Nanofilter array chip for fast gel-free biomolecule separation. Applied Physics Letters 87, 263902-1-3 (2005).
13. Brenner, H. & Edwards, D. A. Macrotransport processes (Butterworth-Heinemann, Boston, 1993).
14. Viovy, J.-L. Electrophoresis of DNA and other polyelectrolytes: Physical mechanisms. Reviews of Modern Physics 72, 813-872 (2000).
15. Meagher, R. J. et al. End-labeled free-solution electrophoresis of DNA. Electrophoresis 26, 331-350 (2005).
16. Zhang, L., Dang, F. & Baba, Y. Microchip electrophoresis-based separation of DNA. Journal of Pharmaceutical and Biomedical Analysis 30, 1645-1654 (2003).
17. Chou, C.-F. et al. Sorting biomolecules with microdevices. Electrophoresis 21, 91-90 (2000).
18. Blom, M. T., Chmela, E., Oosterbroek, R. E., Tijssen, R. & van den Berg, A. On-hip hydrodynamic chromatography separation and detection of nanoparticles and biomolecules. Analytical Chemistry 75, 6761-6768 (2003).
19. Iki, N., Kim, Y. & Yeung, E. S. Electrostatic and Hydrodynamic Separation of DNA Fragments in Capillary Tubes. Analytical Chemistry 68, 4321-4325 (1996).
20. Huang, L. R., Cox, E. C., Austin, R. H. & Sturm, J. C. Continuous particle separation through deterministic lateral displacement. Science 304, 987-990 (2004).
21. Takagi, J., Yamada, m., Yasuda, M. & Seki, M. Continuous particle separation in a microchannel having asymmetrically arranged multiple branches. Lab Chip 5, 778-784 (2005).

22. Bader, J. S. H., Richard w. et al. DNA transport by a micromachined Brownian ratchet device. PNAS 96, 13165-13169 (1999).
23. van Oudenaarden, A. & Boxer, S. Brownian Ratchets: Molecular Separations in Lipid Bilayers Support on Patterned Arrays. Science 285, 1046-1048 (1999).
24. Volkmuth, W. D. & Austin, R. H. DNA electrophoresis in microlithographic arrays. Nature 358, 600-602 (1992).
25. Huang, L. R. et al. A DNA prism for high-speed continuous fractionation of large DNA molecules. Nature 20, 1048-1051 (2002).
26. Han, J. & Craighead, H. G. Separation of Long DNA MOlecules in a Microfabricated Entropic Trap Array. Science 288, 1026-1029 (2000).
27. Fu, J., Mao, P. & Han, J. Nanofilter array chip for fast gel-free biomolecule separation. Applied Physics Letters 87, 293902-1-3 (2005).
28. Fu, J. & Han, J. A nanofilter array chip for fast gel-free biomolecule separation. 9th international conference on miniaturized systems for chemistry and life sciences, 1531-1533 (2005).
29. Mao, P. & Han, J. Fabrication and characterization of 20 nm planar nanofluidic channels by glass-glass and glass-cilicon bonding. Lab Chip 5, 837-844 (2005).
30. LeCoguic, A. & Han, J. Gate Potential Control of Nanofluidic Devices. (2005).
31. Dorfman, K. D. & Brenner, H. Taylor-Aris Dispersion in Microfluidic Networks. (2002).
32. Dorfman, K. D. & Brenner, H. Modeling DNA Electrophoresis in Microfluidic Entropic Trapping Devices. Biomedical Microdevices 4, 237-244 (2002).
33. Stellwagen, N. C., Gelfi, C. & Righetti, P. G. The Free Solution Mobility of DNA. Biopolymers 42, 687-803 (1997).
34. Chen, Y. L. et al. Conformation and dynamics of single DNA molecules in parallel-plate slit microchannels. Physical Review E 70, 060901 (2004).
35. Petersen, N. J., Alarie, J. P., Jacobson, S. C. & Ramsey, J. M. Polyelectrolyte Transport in Nanoconfined Channels. uTAS 7 (2003).
36. Han, S. P. & Yang, S. M. Orientation Distribution and Electrophoretic Motions of Rod-like Particles in a Capillary. Journal of Colloid and Interface Science 177, 132-142 (1996).
37. Giddings, J. C., Kuvera, E., Russel, C. P. & Myers, M. N. Statistical Theory for the Equilibrium Distribution of Rigid Molecules in INert Porous Networks. Exclusion Chromatography. Journal of Physical Chemistry 72, 4397-4408 (1968).
38. Rubenstein, M. & Colby, R. J. Polymer Physics. (2003).
39. Griffiths, S. K. & Nilson, R. H. Band spreading in two-dimensional microchannel turns for electrokinetic species transport. Analytical Chemistry 72, 5473-5482 (2000).
40. http://www.neb.com/nebecomm/products/productN3231.asp.
41. Fu, J., Yoo, J. & Han, J. Molecular sieving in periodic free-energy landscapes created by patterned nanofilter arrays. submitted (2006).
42. Han, J. & Craighead, H. G. Characterization and Optimization of an Entropic Trap for DNA Separation. Analytical Chemistry 74, 394-401 (2001).
43. http://www.neb.com/nebecomm/products/productN3234.asp.
44. Rice, C. L. & Whitehead, R. Electrokinetic Flow in a Narrow Cylindrical Capillary. The Journal of Physical Chemistry 69, 4017-4024 (1965).
45. Tinland, B., Pernodet, N. & Weill, G. Electrophoresis 17, 1046-1051 (1966).
46. Grossman, P. D. & Soane, D. S. Biopolymers 31, 1221-1228 (1991).
47. Lu, Y., Weers, B. & Stellwagen, N. C. DNA Persistence Length Revisited. Biopolymers 61, 261-275 (2002).